EUROPEAN ORGANIZATION FOR NUCLEAR RESEARCH

CERN–EP-2002-082

11 February 2003

A study of the energy evolution of event shape distributions and their means with the DELPHI detector at LEP

DELPHI Collaboration

Abstract

Infrared and collinear safe event shape distributions and their mean values are determined in e^+e^- collisions at centre-of-mass energies between 45 and 202 GeV. A phenomenological analysis based on power correction models including hadron mass effects for both differential distributions and mean values is presented. Using power corrections, α_s is extracted from the mean values and shapes. In an alternative approach, renormalisation group invariance (RGI) is used as an explicit constraint, leading to a consistent description of mean values without the need for sizeable power corrections. The QCD β-function is precisely measured using this approach. From the DELPHI data on Thrust, including data from low energy experiments, one finds

$$\beta_0 = 7.86 \pm 0.32$$

for the one loop coefficient of the β-function or, assuming QCD,

$$n_{\mathrm{f}} = 4.75 \pm 0.44$$

for the number of active flavours. These values agree well with the QCD expectation of $\beta_0 = 7.67$ and $n_{\mathrm{f}} = 5$. A direct measurement of the full logarithmic energy slope excludes light gluinos with a mass below 5 GeV.

(Accepted by Eur.Phys.J.C)

J.Abdallah[25], P.Abreu[22], W.Adam[51], P.Adzic[11], T.Albrecht[17], T.Alderweireld[2], R.Alemany-Fernandez[8], T.Allmendinger[17], P.P.Allport[23], U.Amaldi[29], N.Amapane[45], S.Amato[48], E.Anashkin[36], A.Andreazza[28], S.Andringa[22], N.Anjos[22], P.Antilogus[27], W-D.Apel[17], Y.Arnoud[14], S.Ask[26], B.Asman[44], J.E.Augustin[25], A.Augustinus[8], P.Baillon[8], A.Ballestrero[46], P.Bambade[20], R.Barbier[27], D.Bardin[16], G.Barker[17], A.Baroncelli[39], M.Battaglia[8], M.Baubillier[25], K-H.Becks[53], M.Begalli[6], A.Behrmann[53], E.Ben-Haim[20], N.Benekos[32], A.Benvenuti[5], C.Berat[14], M.Berggren[25], L.Berntzon[44], D.Bertrand[2], M.Besancon[40], N.Besson[40], D.Bloch[9], M.Blom[31], M.Bluj[52], M.Bonesini[29], M.Boonekamp[40], P.S.L.Booth[23], G.Borisov[21], O.Botner[49], B.Bouquet[20], T.J.V.Bowcock[23], I.Boyko[16], M.Bracko[43], R.Brenner[49], E.Brodet[35], P.Bruckman[18], J.M.Brunet[7], L.Bugge[33], P.Buschmann[53], M.Calvi[29], T.Camporesi[8], V.Canale[38], F.Carena[8], N.Castro[22], F.Cavallo[5], M.Chapkin[42], Ph.Charpentier[8], P.Checchia[36], R.Chierici[8], P.Chliapnikov[42], J.Chudoba[8], S.U.Chung[8], K.Cieslik[18], P.Collins[8], R.Contri[13], G.Cosme[20], F.Cossutti[47], M.J.Costa[50], B.Crawley[1], D.Crennell[37], J.Cuevas[34], J.D'Hondt[2], J.Dalmau[44], T.da Silva[48], W.Da Silva[25], G.Della Ricca[47], A.De Angelis[47], W.De Boer[17], C.De Clercq[2], B.De Lotto[47], N.De Maria[45], A.De Min[36], L.de Paula[48], L.Di Ciaccio[38], A.Di Simone[39], K.Doroba[52], J.Drees[53,8], M.Dris[32], G.Eigen[4], T.Ekelof[49], M.Ellert[49], M.Elsing[8], M.C.Espirito Santo[22], G.Fanourakis[11], D.Fassouliotis[11,3], M.Feindt[17], J.Fernandez[41], A.Ferrer[50], F.Ferro[13], U.Flagmeyer[53], H.Foeth[8], E.Fokitis[32], F.Fulda-Quenzer[20], J.Fuster[50], M.Gandelman[48], C.Garcia[50], Ph.Gavillet[8], E.Gazis[32], R.Gokieli[8,52], B.Golob[43], G.Gomez-Ceballos[41], P.Goncalves[22], E.Graziani[39], G.Grosdidier[20], K.Grzelak[52], J.Guy[37], C.Haag[17], A.Hallgren[49], K.Hamacher[53], K.Hamilton[35], J.Hansen[33], S.Haug[33], F.Hauler[17], V.Hedberg[26], M.Hennecke[17], H.Herr[8], J.Hoffman[52], S-O.Holmgren[44], P.J.Holt[8], M.A.Houlden[23], K.Hultqvist[44], J.N.Jackson[23], G.Jarlskog[26], P.Jarry[40], D.Jeans[35], E.K.Johansson[44], P.D.Johansson[44], P.Jonsson[27], C.Joram[8], L.Jungermann[17], F.Kapusta[25], S.Katsanevas[27], E.Katsoufis[32], G.Kernel[43], B.P.Kersevan[8,43], A.Kiiskinen[15], B.T.King[23], N.J.Kjaer[8], P.Kluit[31], P.Kokkinias[11], C.Kourkoumelis[3], O.Kouznetsov[16], Z.Krumstein[16], M.Kucharczyk[18], J.Lamsa[1], G.Leder[51], F.Ledroit[14], L.Leinonen[44], R.Leitner[30], J.Lemonne[2], V.Lepeltier[20], T.Lesiak[18], W.Liebig[53], D.Liko[51], A.Lipniacka[44], J.H.Lopes[48], J.M.Lopez[34], D.Loukas[11], P.Lutz[40], L.Lyons[35], J.MacNaughton[51], A.Malek[53], S.Maltezos[32], F.Mandl[51], J.Marco[41], R.Marco[41], B.Marechal[48], M.Margoni[36], J-C.Marin[8], C.Mariotti[8], A.Markou[11], C.Martinez-Rivero[41], J.Masik[12], N.Mastroyiannopoulos[11], F.Matorras[41], C.Matteuzzi[29], F.Mazzucato[36], M.Mazzucato[36], R.Mc Nulty[23], C.Meroni[28], W.T.Meyer[1], E.Migliore[45], W.Mitaroff[51], U.Mjoernmark[26], T.Moa[44], M.Moch[17], K.Moenig[8,10], R.Monge[13], J.Montenegro[31], D.Moraes[48], S.Moreno[22], P.Morettini[13], U.Mueller[53], K.Muenich[53], M.Mulders[31], L.Mundim[6], W.Murray[37], B.Muryn[19], G.Myatt[35], T.Myklebust[33], M.Nassiakou[11], F.Navarria[5], K.Nawrocki[52], R.Nicolaidou[40], M.Nikolenko[16,9], A.Oblakowska-Mucha[19], V.Obraztsov[42], A.Olshevski[16], A.Onofre[22], R.Orava[15], K.Osterberg[15], A.Ouraou[40], A.Oyanguren[50], M.Paganoni[29], S.Paiano[5], J.P.Palacios[23], H.Palka[18], Th.D.Papadopoulou[32], L.Pape[8], C.Parkes[24], F.Parodi[13], U.Parzefall[8], A.Passeri[39], O.Passon[53], L.Peralta[22], V.Perepelitsa[50], A.Perrotta[5], A.Petrolini[13], J.Piedra[41], L.Pieri[39], F.Pierre[40], M.Pimenta[22], E.Piotto[8], T.Podobnik[43], V.Poireau[8], M.E.Pol[6], G.Polok[18], P.Poropat[†47], V.Pozdniakov[16], N.Pukhaeva[2,16], A.Pullia[29], J.Rames[12], L.Ramler[17], A.Read[33], P.Rebecchi[8], J.Rehn[17], D.Reid[31], R.Reinhardt[53], P.Renton[35], F.Richard[20], J.Ridky[12], M.Rivero[41], D.Rodriguez[41], A.Romero[45], P.Ronchese[36], E.Rosenberg[1], P.Roudeau[20], T.Rovelli[5], V.Ruhlmann-Kleider[40], D.Ryabtchikov[42], A.Sadovsky[16], L.Salmi[15], J.Salt[50], A.Savoy-Navarro[25], U.Schwickerath[8], A.Segar[35], R.Sekulin[37], M.Siebel[53], A.Sisakian[16], G.Smadja[27], O.Smirnova[26], A.Sokolov[42], A.Sopczak[21], R.Sosnowski[52], T.Spassov[8], M.Stanitzki[17], A.Stocchi[20], J.Strauss[51], B.Stugu[4], M.Szczekowski[52], M.Szeptycka[52], T.Szumlak[19], T.Tabarelli[29], A.C.Taffard[23], F.Tegenfeldt[49], J.Timmermans[31], L.Tkatchev[16], M.Tobin[23], S.Todorovova[12], B.Tome[22], A.Tonazzo[29], P.Tortosa[50], P.Travnicek[12], D.Treille[8], G.Tristram[7], M.Trochimczuk[52], C.Troncon[28], M-L.Turluer[40], I.A.Tyapkin[16], P.Tyapkin[16], S.Tzamarias[11], V.Uvarov[42], G.Valenti[5], P.Van Dam[31], J.Van Eldik[8], A.Van Lysebetten[2], N.van Remortel[2], I.Van Vulpen[8], G.Vegni[28], F.Veloso[22], W.Venus[37], F.Verbeure[2], P.Verdier[27], V.Verzi[38], D.Vilanova[40], L.Vitale[47], V.Vrba[12], H.Wahlen[53], A.J.Washbrook[23],

C.Weiser[17], D.Wicke[8], J.Wickens[2], G.Wilkinson[35], M.Winter[9], M.Witek[18], O.Yushchenko[42], A.Zalewska[18], P.Zalewski[52], D.Zavrtanik[43], V.Zhuravlov[16], N.I.Zimin[16], A.Zintchenko[16], M.Zupan[11]

[1]Department of Physics and Astronomy, Iowa State University, Ames IA 50011-3160, USA
[2]Physics Department, Universiteit Antwerpen, Universiteitsplein 1, B-2610 Antwerpen, Belgium
and IIHE, ULB-VUB, Pleinlaan 2, B-1050 Brussels, Belgium
and Faculté des Sciences, Univ. de l'Etat Mons, Av. Maistriau 19, B-7000 Mons, Belgium
[3]Physics Laboratory, University of Athens, Solonos Str. 104, GR-10680 Athens, Greece
[4]Department of Physics, University of Bergen, Allégaten 55, NO-5007 Bergen, Norway
[5]Dipartimento di Fisica, Università di Bologna and INFN, Via Irnerio 46, IT-40126 Bologna, Italy
[6]Centro Brasileiro de Pesquisas Físicas, rua Xavier Sigaud 150, BR-22290 Rio de Janeiro, Brazil
and Depto. de Física, Pont. Univ. Católica, C.P. 38071 BR-22453 Rio de Janeiro, Brazil
and Inst. de Física, Univ. Estadual do Rio de Janeiro, rua São Francisco Xavier 524, Rio de Janeiro, Brazil
[7]Collège de France, Lab. de Physique Corpusculaire, IN2P3-CNRS, FR-75231 Paris Cedex 05, France
[8]CERN, CH-1211 Geneva 23, Switzerland
[9]Institut de Recherches Subatomiques, IN2P3 - CNRS/ULP - BP20, FR-67037 Strasbourg Cedex, France
[10]Now at DESY-Zeuthen, Platanenallee 6, D-15735 Zeuthen, Germany
[11]Institute of Nuclear Physics, N.C.S.R. Demokritos, P.O. Box 60228, GR-15310 Athens, Greece
[12]FZU, Inst. of Phys. of the C.A.S. High Energy Physics Division, Na Slovance 2, CZ-180 40, Praha 8, Czech Republic
[13]Dipartimento di Fisica, Università di Genova and INFN, Via Dodecaneso 33, IT-16146 Genova, Italy
[14]Institut des Sciences Nucléaires, IN2P3-CNRS, Université de Grenoble 1, FR-38026 Grenoble Cedex, France
[15]Helsinki Institute of Physics, P.O. Box 64, FIN-00014 University of Helsinki, Finland
[16]Joint Institute for Nuclear Research, Dubna, Head Post Office, P.O. Box 79, RU-101 000 Moscow, Russian Federation
[17]Institut für Experimentelle Kernphysik, Universität Karlsruhe, Postfach 6980, DE-76128 Karlsruhe, Germany
[18]Institute of Nuclear Physics,Ul. Kawiory 26a, PL-30055 Krakow, Poland
[19]Faculty of Physics and Nuclear Techniques, University of Mining and Metallurgy, PL-30055 Krakow, Poland
[20]Université de Paris-Sud, Lab. de l'Accélérateur Linéaire, IN2P3-CNRS, Bât. 200, FR-91405 Orsay Cedex, France
[21]School of Physics and Chemistry, University of Lancaster, Lancaster LA1 4YB, UK
[22]LIP, IST, FCUL - Av. Elias Garcia, 14-1^{o}, PT-1000 Lisboa Codex, Portugal
[23]Department of Physics, University of Liverpool, P.O. Box 147, Liverpool L69 3BX, UK
[24]Dept. of Physics and Astronomy, Kelvin Building, University of Glasgow, Glasgow G12 8QQ
[25]LPNHE, IN2P3-CNRS, Univ. Paris VI et VII, Tour 33 (RdC), 4 place Jussieu, FR-75252 Paris Cedex 05, France
[26]Department of Physics, University of Lund, Sölvegatan 14, SE-223 63 Lund, Sweden
[27]Université Claude Bernard de Lyon, IPNL, IN2P3-CNRS, FR-69622 Villeurbanne Cedex, France
[28]Dipartimento di Fisica, Università di Milano and INFN-MILANO, Via Celoria 16, IT-20133 Milan, Italy
[29]Dipartimento di Fisica, Univ. di Milano-Bicocca and INFN-MILANO, Piazza della Scienza 2, IT-20126 Milan, Italy
[30]IPNP of MFF, Charles Univ., Areal MFF, V Holesovickach 2, CZ-180 00, Praha 8, Czech Republic
[31]NIKHEF, Postbus 41882, NL-1009 DB Amsterdam, The Netherlands
[32]National Technical University, Physics Department, Zografou Campus, GR-15773 Athens, Greece
[33]Physics Department, University of Oslo, Blindern, NO-0316 Oslo, Norway
[34]Dpto. Fisica, Univ. Oviedo, Avda. Calvo Sotelo s/n, ES-33007 Oviedo, Spain
[35]Department of Physics, University of Oxford, Keble Road, Oxford OX1 3RH, UK
[36]Dipartimento di Fisica, Università di Padova and INFN, Via Marzolo 8, IT-35131 Padua, Italy
[37]Rutherford Appleton Laboratory, Chilton, Didcot OX11 OQX, UK
[38]Dipartimento di Fisica, Università di Roma II and INFN, Tor Vergata, IT-00173 Rome, Italy
[39]Dipartimento di Fisica, Università di Roma III and INFN, Via della Vasca Navale 84, IT-00146 Rome, Italy
[40]DAPNIA/Service de Physique des Particules, CEA-Saclay, FR-91191 Gif-sur-Yvette Cedex, France
[41]Instituto de Fisica de Cantabria (CSIC-UC), Avda. los Castros s/n, ES-39006 Santander, Spain
[42]Inst. for High Energy Physics, Serpukov P.O. Box 35, Protvino, (Moscow Region), Russian Federation
[43]J. Stefan Institute, Jamova 39, SI-1000 Ljubljana, Slovenia and Laboratory for Astroparticle Physics,
Nova Gorica Polytechnic, Kostanjeviska 16a, SI-5000 Nova Gorica, Slovenia,
and Department of Physics, University of Ljubljana, SI-1000 Ljubljana, Slovenia
[44]Fysikum, Stockholm University, Box 6730, SE-113 85 Stockholm, Sweden
[45]Dipartimento di Fisica Sperimentale, Università di Torino and INFN, Via P. Giuria 1, IT-10125 Turin, Italy
[46]INFN,Sezione di Torino, and Dipartimento di Fisica Teorica, Università di Torino, Via P. Giuria 1,
IT-10125 Turin, Italy
[47]Dipartimento di Fisica, Università di Trieste and INFN, Via A. Valerio 2, IT-34127 Trieste, Italy
and Istituto di Fisica, Università di Udine, IT-33100 Udine, Italy
[48]Univ. Federal do Rio de Janeiro, C.P. 68528 Cidade Univ., Ilha do Fundão BR-21945-970 Rio de Janeiro, Brazil
[49]Department of Radiation Sciences, University of Uppsala, P.O. Box 535, SE-751 21 Uppsala, Sweden
[50]IFIC, Valencia-CSIC, and D.F.A.M.N., U. de Valencia, Avda. Dr. Moliner 50, ES-46100 Burjassot (Valencia), Spain
[51]Institut für Hochenergiephysik, Österr. Akad. d. Wissensch., Nikolsdorfergasse 18, AT-1050 Vienna, Austria
[52]Inst. Nuclear Studies and University of Warsaw, Ul. Hoza 69, PL-00681 Warsaw, Poland
[53]Fachbereich Physik, University of Wuppertal, Postfach 100 127, DE-42097 Wuppertal, Germany
† deceased

1 Introduction

The decrease of the strong coupling parameter, α_s, with increasing energy, E, or momentum transfer, Q, and the related properties of asymptotic freedom and confinement are striking phenomena of Quantum Chromodynamics, QCD, the gauge theory of strong interactions. Besides the measurement of the strong coupling itself, the precise measurement of its energy dependence is an experimental task of fundamental importance. This energy dependence is governed by the β function, defined as [1]:

$$\begin{aligned} Q\frac{\mathrm{d}\alpha_\mathrm{s}}{\mathrm{dQ}} &= \beta(\alpha_s) \qquad (1)\\ &= -\frac{\beta_0}{2\pi}\alpha_s^2 - \frac{\beta_1}{4\pi^2}\alpha_s^3 - \frac{\beta_2}{64\pi^3}\alpha_s^4 - \cdots \end{aligned}$$

The coefficients β_i are given in the Equations 14.

In principle, the study of event shape observables (e.g. Thrust) in $\mathrm{e^+e^-}$ annihilation as a function of energy permits these determinations. Event shape observables, however, are obscured by the effects of non–perturbative hadronisation. This influence is expected to vanish with increasing energy (going dominantly proportional to $1/E$). A similar dependence is present in the so-called infrared renormalons appearing in perturbation theory [2]. Both phenomena are often considered to originate from the same physics.

The theoretical analysis of power terms indicates some properties which are universal to all observables. A coherent comparison of the power correction models and the proposed universality is one topic of this paper.

Power corrections are subject to ambiguities. They depend on the borderline dividing perturbative and non–perturbative physics in the models; this borderline is a matter of convention. Usually the perturbative terms are treated in an $\mathcal{O}(\alpha_s^2)$ approximation, the remainder being taken as a power correction. The inclusion of higher order perturbative corrections in general will reduce the size of the power terms.

Power correction models are now considered as established. However, in view of a precise measurement of the strong coupling, power corrections and the ambiguity involved are obstructive. Quantities for which power corrections are minimised should be emphasised. Moreover the reason for the success of power corrections and their magnitudes is "not yet fully understood" [3]. Hence a critical review of other theoretical methods for many experimental observables is in order.

The second focus of the phenomenological analysis presented in this paper is on the study of renormalisation group invariant perturbation theory (RGI) [4–6]. Here the property of complete renormalisation group invariance is used, leading to predictions without the freedom arising from the choice of renormalisation scheme or scale. The theoretical ansatz employed [5], however, only applies to "fully inclusive" observables depending on a single energy scale, such as total cross–sections [7,8], or mean values of event shape observables. A thorough test of this theoretical method is presented here based on the energy dependence of the means of the distributions of seven event shape observables. The convincing success of this test implies that the size of the power corrections found for the power correction models in the $\overline{MS}$ renormalisation scheme can be predicted using RGI perturbation theory. Furthermore RGI perturbation theory allows a direct measurement of the β-function of QCD avoiding any scheme dependence.

Since the goal of this analysis is a study of the scale dependence, data with a wide range of centre–of–mass energies are needed. Therefore data have been used from the high energy running of LEP up to centre-of-mass energies of 202 GeV, from the energies

around the Z pole, and also radiative events with a reduced centre-of-mass energy of the hadronic system due to hard photon radiation. Additionally for some part of the analysis low energy data from other experiments are included.

The organisation of this paper is as follows: Section 2 discusses briefly the apparatus, the data and the analysis of the LEP2 data and the radiative events used to extract data below the Z mass scale. The observables used throughout the paper are introduced and their dependence on the masses of the final state hadrons is discussed. Finally, procedures to determine systematic uncertainties are specified. Section 3 presents the data on shape distributions and their means and compares them to predictions of prominent fragmentation models. Section 4 similarly makes comparisons with analytic power model predictions [9–11], together with a comparison of the non–perturbative parameters for the different observables. For the first time the prediction of power corrections for the energy-energy correlation (EEC) is compared to experimental data and evidence for power shifts at the three jet phase space boundary is given. Section 5 contains the power correction analysis for mean values of exponentiating event shape observables based on the prescription of [12,13]. Simple power fits [14,15] are then presented for all shape observable means and it is shown that the size of the power terms correlates with that of the corresponding second order perturbative contribution. Section 6 briefly recalls the basics of the RGI method as given in [5] and confronts it with the data on shape observable means. It is shown that this method describes the data very well. The inclusion of power terms in the fit shows no indication of significant non–perturbative effects. Consequently the size of the power terms determined in the previous chapter is estimated from the RGI method and shown to agree with experimental data. By applying the RGI method to different shape observable means as measured by DELPHI, especially to the data on $\langle 1 - \text{Thrust} \rangle$ combined with results of other experiments at low energy, a direct precise measurement of the QCD β-function is obtained. Finally we summarise and conclude in Section 7.

2 Detector, data and data analysis

DELPHI is a hermetic detector with a solenoidal magnetic field of 1.2T. The tracking detectors, situated in front of the electro-magnetic calorimeters are a silicon micro-vertex detector (VD), a combined jet/proportional chamber inner detector (ID), a time projection chamber (TPC) as the major tracking device, and the streamer tube detector OD in the barrel region. The forward region is covered by silicon mini-strip and pixel detectors (VFT) and by the drift chamber detectors FCA and FCB.

The electromagnetic calorimeters are the high density projection chamber HPC in the barrel, and the lead-glass calorimeter FEMC in the forward region. Detailed information about the design and performance of DELPHI can be found in [16,17].

The phenomenological analysis of the event shape data presented in the following sections relies on the DELPHI data measured at the Z-peak, the off-peak energies of 89 and 93 GeV, as well as the published data between the Z peak and 183 GeV[18,19]. In addition the data measured at centre-of-mass energies $\sqrt{s}$ between 189 and 202 GeV and from radiative events at mean hadronic centre-of-mass energies of 45, 66 and 78 GeV are presented. The number of events accepted in the analysis at these energies and the integrated luminosities collected are given in Table 1.

E_{cm}	σ	σ_{eff}	$\mathcal{L}$	N_{sel}	ϵ	p
[GeV]	$[pb]$	$[pb]$	$[pb^{-1}]$			
45.2	-	-	-	650	0.255	0.842
66.0	-	-	-	1099	0.283	0.913
76.3	-	-	-	1212	0.238	0.876
89.4	9656.	9509.	17.0	$148 \cdot 10^3$	0.843	0.998
91.3	30486.	30080.	92.3	$2.5 \cdot 10^6$	0.845	0.999
93.0	14007.	13757.	18.6	$230 \cdot 10^3$	0.844	0.999
133.2	291.	69.2	11.9	850	0.958	0.999
161.4	147.	32.3	10.1	282	0.711	0.992
172.3	121.	27.5	9.9	219	0.729	0.956
183.1	100.	23.4	54.0	1035	0.733	0.930
189.2	99.8	21.1	150.7	2774	0.749	0.909
192.2	96.0	20.2	25.8	433	0.757	0.889
196.2	90.0	19.2	77.5	1288	0.754	0.876
200.1	85.2	18.2	80.9	1281	0.767	0.857
202.1	83.3	17.7	40.0	624	0.764	0.890

Table 1: Nominal centre-of-mass energies E_{cm}, cross–sections, without (σ), and with ISR cut (σ_{eff}), luminosities ($\mathcal{L}$), the number of selected events (N_{sel}), the efficiencies (ϵ) and the purities (p).

2.1 Selection and analysis of high energy data

In order to select well measured particles, the cuts given in the upper part of Table 2 have been applied. The cuts in the lower part of the table are used to select $\mathrm{e^+e^-} \to \mathrm{Z}/\gamma \to \mathrm{q\bar{q}}$ events and to suppress background processes such as two-photon interactions, beam-gas and beam-wall interactions, leptonic final states and, for the LEP2 analysis, initial state radiation (ISR) and four-fermion background.

At energies above 91.2 GeV, the high cross–section of the Z resonance peak raises the possibility of hard ISR allowing the creation of a nearly on–shell Z boson. These "radiative return events" constitute a large fraction of all hadronic events. The initial state photons are typically aligned along the beam direction and are rarely identified inside the detector. In order to evaluate the effective hadronic centre-of-mass energy $\sqrt{s'_{rec}}$ of an event, taking ISR into account, the procedure described in [20] was applied. It is based on a fit imposing four–momentum conservation to measured jet four–momenta (including estimates of their uncertainties). Several assumptions about the event topology are tested. The decision is taken according to the χ^2 obtained from the constrained fits with different topologies.

Figure 1 shows the spectrum of the calculated energies for simulated and measured events passing all but the $\sqrt{s'_{rec}}$ cut for 200 GeV $\mathrm{e^+e^-}$ centre-of-mass energy. The agreement between data and simulation is good for the high energies relevant to this analysis, while the peak around M_{Z} appears to be slightly shifted in the simulation. A cut requiring the reconstructed centre-of-mass energy $\sqrt{s'_{rec}}$ to be greater than $0.9 \cdot E_{cm}$ is applied to discard radiative return events (see Table 2).

Two photon events are strongly suppressed by the cuts. Leptonic background was found to be negligible in this analysis.

neutral particle selection	$E \geq 0.5\,\mathrm{GeV}$ $20^\circ \leq \theta \leq 160^\circ$
charged particle selection	$0.4\,\mathrm{GeV} \leq p \leq 100\,\mathrm{GeV}$ $\Delta p/p \leq 1.0$ measured track length ≥ 30 cm distance to I.P. in $r\phi$ plane ≤ 4 cm distance to I.P. in $z \leq 10$ cm $20^\circ < \theta < 160^\circ$
Standard event selection	$N_{\mathrm{ch}} \geq 7$ $30^\circ \leq \theta_{\mathrm{Thrust}} \leq 150^\circ$ $E_{\mathrm{tot}} \geq 0.50 E_{\mathrm{cm}}$
ISR cuts	$\sqrt{s'_{\mathrm{rec}}} \geq 90\% E_{\mathrm{cm}}$
WW cuts	$N_{\mathrm{ch}} > 500 \cdot B_{\mathrm{min}} + 1.5$ $N_{\mathrm{ch}} \leq 42$
prompt photon selection	$E_\gamma - 10\,\mathrm{GeV} < E_W < E_\gamma + 5\,\mathrm{GeV}$ $11\,\mathrm{GeV} < E_\gamma < E_{\mathrm{cm}}/2$ $\alpha_\gamma = 25^\circ$ $E_\alpha < 0.5\,\mathrm{GeV}$

Table 2: Selection of particles and events. E is the energy, p is the momentum, Δp its error, r the distance to the beam-axis, z the distance to the beam interaction point (I.P.) along the beam-axis, ϕ and θ the azimuthal and polar angles with respect to the beam, N_{ch} the number of charged particles, θ_{Thrust} the polar angle of the Thrust axis with respect to the beam, E_{tot} the total energy carried by all particles, E_{cm} ther nominal LEP energy, $\sqrt{s'_{\mathrm{rec}}}$ the reconstructed hadronic centre-of-mass energy, B_{min} is the minimal Jet Broadening (described in Section 2.3), E_γ the energy of the detected photon, E_W the angular energy (see Equation 3), a_γ the opening angle of the photon isolation cone and E_α the maximum additional energy deposit within this cone.

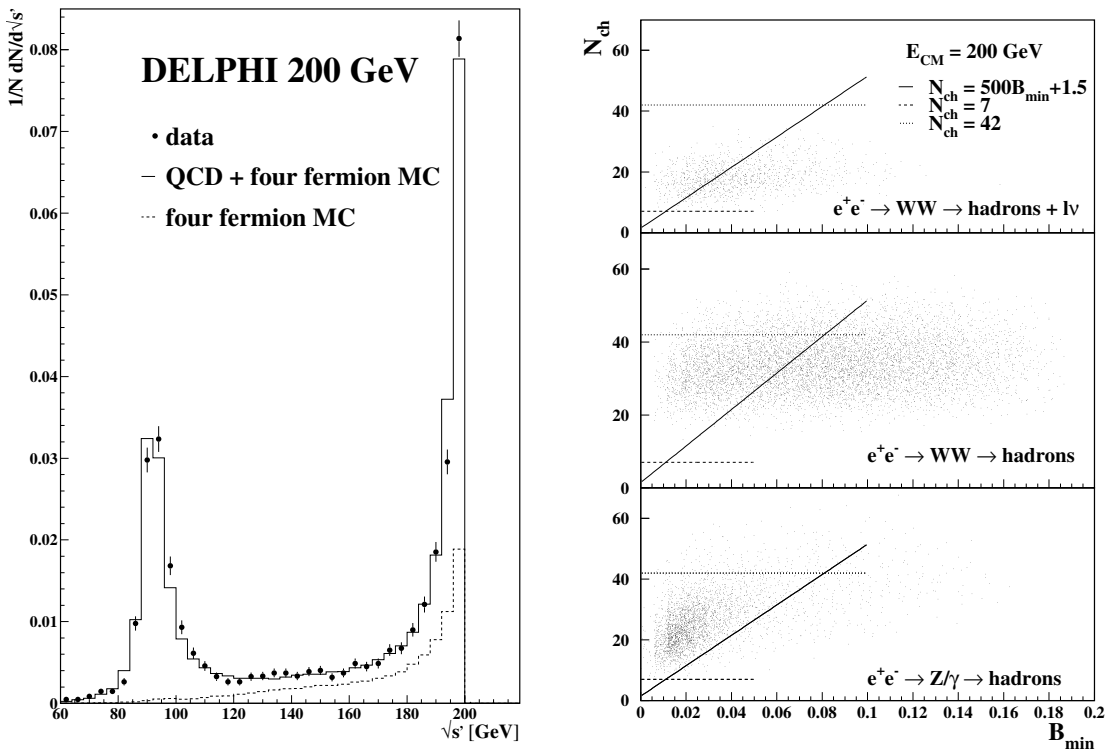

Figure 1: Left: Reconstructed centre-of-mass energy for accepted data before $\sqrt{s'}$ cut compared to QCD and four-fermion simulation. Right: Simulation of four-fermion background and QCD events in the N_{ch}–B_{min} plane. The upper two plots show the distributions for semi–leptonic and fully hadronic WW events, respectively. The lines indicate the cut values chosen.

Since the topological signatures of QCD four-jet events and four-fermion backgrounds such as hadronically decaying ZZ or WW events are similar, no highly efficient separation of these two classes of events is possible. Thus any four-fermion rejection implies a severe bias to the shape distributions of QCD events, which needs to be corrected with simulation. By applying a cut on an observable calculated from the narrow event hemisphere only (like B_{min}, see Section 2.3), the bias to event shape observables mainly sensitive to the wide event hemisphere is reduced. The two dimensional cut in the N_{ch}–B_{min} plane exploits the different correlation between these observables in QCD and four-fermion events (see Figure 1). Applying the two dimensional cut almost 90% of the four-fermion background can be suppressed. The remaining four-fermion contribution is estimated by Monte Carlo generators and subtracted from the measurement. The remaining detector and cut effects are unfolded with simulation. The influence of detector effects was studied by passing generated events (JETSET/PYTHIA [21] using the DELPHI tuning described in [22]) through a full detector simulation (DELSIM [16]). These simulated events are processed with the same reconstruction program and selection cuts as are the real data. In order to correct for cuts, detector, and ISR effects a bin-by-bin acceptance correction C, obtained from $\mathrm{e^+e^-} \to \mathrm{Z}/\gamma \to \mathrm{q\bar{q}}$ simulation, is applied to the data:

$$C_i = \frac{h(f_i)_{\mathrm{gen,noISR}}}{h(f_i)_{\mathrm{acc}}} \quad , \tag{2}$$

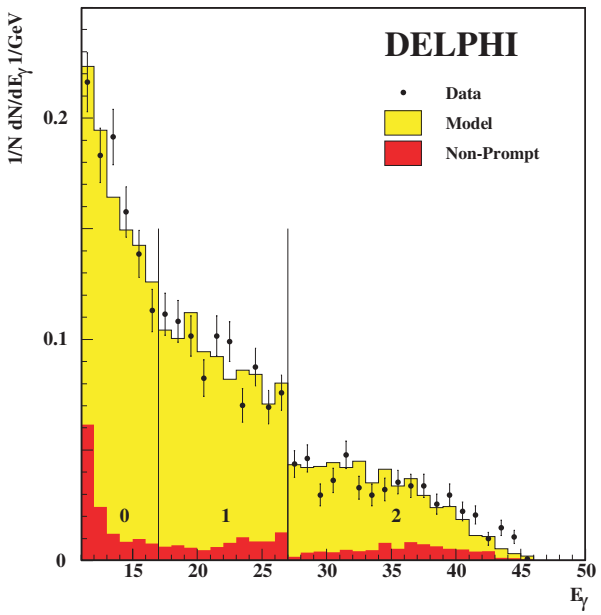

Figure 2: The energy distribution of the photon in the selected isolated photon events. The three classes (0,1,2) correspond to a mean centre-of-mass energy of 76, 66 and 45 GeV, respectively. The steps between the classes result from different π^0 rejection cuts.

where $h(f_i)_{\mathrm{gen,noISR}}$ represents the contents of bin i of the shape distribution f generated with the tuned generator. The calculation includes all stable particles. The subscript noISR indicates that only events without significant ISR ($\sqrt{s} - \sqrt{s'} < 0.1\,\mathrm{GeV}$) enter the distribution. $h(f_i)_{\mathrm{acc}}$ represents the accepted distribution f as obtained with the full detector simulation.

2.2 Data selection at hadronic centre-of-mass energies below M_{Z}

In order to extend the available energy range below the Z-peak, events with reduced hadronic centre-of-mass energies due to hard photon radiation are selected from data taken at centre-of-mass energy of 91 GeV in 1992 through 95. The method requires an energetic isolated photon to be detected and is based on the hypothesis that such photons are emitted before or immediately after the Z/γ interaction [23] and do not interfere with the QCD fragmentation processes. The angular distribution of the initial state radiation is aligned along the direction of the beams, with the result, that most photons go undetected in the very forward region. In contrast, photons from final state radiation tend to be grouped along the direction of the final state partons and can be detected with better efficiency. As a result the selected events are dominated by final state radiation.

Many of the photons convert into $\mathrm{e^+e^-}$ pairs in the material before the calorimeter. These are reconstructed using the tracking detector information left by the $\mathrm{e^+}$ and $\mathrm{e^-}$ particles. Only the reconstructed conversions before the TPC with electron and positron measurements in the TPC and conversions behind the TPC with electron and positron measurements in the OD or the HPC are used.

The largest part of the non-photonic background stems from π^0's decaying into two photons. Due to the high granularity of the HPC the photon shower can be tested for a two photon hypothesis. This is done by two methods. The first tries to divide the cluster into two subclusters and reconstructs the invariant mass of the decayed particle. The second measures the asymmetry of the energy distribution in the $\theta\phi$-plane, as two photons generate a more elliptic cluster shape. The results of these two methods are combined in a single probabilistic variable. Since the angle between the two photons decreases with the energy, harder cuts had to be made for higher photon energies.

In order to distinguish prompt photons from soft collinear photons arising in the later stages of fragmentation and decays, hard cuts on the photon energy and the isolation with respect to other jets have to be applied. Isolation is defined by two criteria. In order to obtain photons at a large angle with respect to the final state particle a minimum angle of 20° to the jet axes is demanded. The jets are defined by the Durham cluster algorithm with $y_{\rm cut} = 0.06$. The additional energy deposition within a 25° cone around the jet–axis had to be less than 0.5 GeV, which reduces background from π^0 decays. Electromagnetic punch-through entering the HCAL has been considered.

To test the consistency of the measured photon energy, the following cross–check is performed: the event, exluding the photon, is clustered into two jets and the energy of the radiative photon is reconstructed from the angles between jets j,k and photon i through the following equation:

$$E_{\rm W} = \frac{|\sin\theta_{jk}|}{|\sin\theta_{ji}| + |\sin\theta_{ik}| + |\sin\theta_{jk}|} E_{cm} \quad . \tag{3}$$

This reconstructed energy is required to coincide with the photon energy measured by the calorimeters in the range $E_\gamma - 10\,{\rm GeV} < E_{\rm W} < E_\gamma + 5\,{\rm GeV}$.

The additional selection criteria for ISR and final state radiation (FSR) events are summarised in Table 2. The energy distribution of the final prompt photon candidates can be seen in Figure 2. From selected events the tagged photon is removed, and the event is boosted into the centre-of-mass frame of the hadronic system. The boost was determined by the measured photon. The events are summed up into three intervals in centre-of-mass energy. The mean value of each sample is taken as the nominal energy as calculated using the measured radiated photon and a correction is applied.

2.3 Observables and their mass corrections

The event shape observables used throughout this paper are calculated from the charged and neutral particles.

The Thrust T [24] is defined by

$$T = \frac{\sum_{k=1}^{N} |\vec{p}_k \cdot \vec{n}_T|}{\sum_{k=1}^{N} |\vec{p}_k|} \quad , \tag{4}$$

where $\vec{p}_i$ is the momentum vector of particle i and $\vec{n}_T$ is the Thrust axis, which maximizes the above expression. The observable Major is defined similarly, replacing $\vec{n}_T$ with $\vec{n}_M$ which is constrained to be perpendicular to $\vec{n}_T$. The C-parameter[25] is defined by the eigenvalues λ of the infrared-safe linear momentum tensor Θ^{ij}:

$$\Theta^{ij} = \frac{1}{\sum_{k=1}^{N} |\vec{p}_k|} \sum_{k=1}^{N} \frac{p_k^i p_k^j}{|\vec{p}_k|} \qquad C = 3(\lambda_1\lambda_2 + \lambda_2\lambda_3 + \lambda_3\lambda_1) \quad . \tag{5}$$

Here p_k^i denotes the i-component of $\vec{p}_k$. Events can be divided into two hemispheres, positive and negative, by the plane perpendicular to the Thrust axis $\vec{n}_T$. The so–called Jet Masses [26] are then given by

$$M_\pm^2 = \left(\sum_{\pm\vec{p}_k\cdot\vec{n}_T>0} p_k \right)^2 \quad , \qquad M_{\rm h}^2 = \max(M_+^2, M_-^2) \quad , \qquad M_{\rm s}^2 = M_+^2 + M_-^2 \quad . \tag{6}$$

The Jet Broadenings [27] are defined by summing the transverse momenta of the particles:

$$B_\pm = \frac{1}{2\sum_{k=1}^N |\vec{p}_k|} \sum_{\pm\vec{p}_k\cdot\vec{n}_{\rm T}>0} |\vec{p}_k \times \vec{n}_{\rm T}| \quad , \quad B_{\rm max} = \max(B_-, B_+) \quad , \quad B_{\rm sum} = B_- + B_+ \quad . \tag{7}$$

The energy-energy correlation EEC [28] measures the correlation of the energy flow in an hadronic event. It is defined as

$$\frac{d\Sigma(\chi)}{d\cos\chi} = \frac{1}{N}\frac{\sigma}{\Delta\cos\chi} \sum_{N_{\rm Evt.}} \sum_{ij}^{particles} \frac{E_i E_j}{E_{\rm vis}^2} \int_{\cos\chi-\frac{\Delta\cos\chi}{2}}^{\cos\chi+\frac{\Delta\cos\chi}{2}} \delta(\rho - \cos\chi_{ij}) d\rho \quad . \tag{8}$$

Here χ_{ij} denotes the angle between the particles i and j. The jet cone energy fraction JCEF [29] integrates the energy within a conical shell of average half-angle χ around the Thrust axis. It is defined as

$$JCEF(\chi) = \frac{1}{N}\frac{1}{\Delta\chi} \sum_N \sum_i \frac{E_i}{E_{\rm vis}} \int_{\chi-\frac{\Delta\chi}{2}}^{\chi+\frac{\Delta\chi}{2}} \delta(\chi' - \chi_i) d\chi' \quad , \tag{9}$$

where χ_i is the opening angle between a particle and the Thrust axis pointing in the direction of the light Jet Mass hemisphere:

$$\chi_i = \cos^{-1}\left(\frac{\vec{p}_i \cdot \vec{n}_T}{|\vec{p}_i|}\right) \quad . \tag{10}$$

Evidently the statistical correlation between the event shape observables when calculated from the same data is very high. But since their QCD predictions are different (e.g. the relative size of the second order contributions) studying them provides an important cross–check for QCD.

In the subsequent analysis QCD effects are calculated in the massless limit. This is an approximation which can lead to substantial deviations for some sensitive observables in certain cases and in the low energy limit in general. In order to reduce mass effects two approaches are applied: In [30] it is proposed that hadron masses are associated with corrections that are proportional to $(\ln Q)^A/Q$ with $A \simeq 1.6$, which can be of the same size as traditional power corrections. The mass induced power corrections can be separated into two classes, universal and non-universal, where the non-universal can be reduced by a redefinition of the observables. The Jet Masses in particular are subject to large mass corrections. To suppress the influence of the hadron masses, new observables were defined which for massless hadrons are identical to the standard $M_{\rm h}^2/E_{\rm vis}^2$–definition [30]. They are defined by replacing the four–momentum p in the standard formula:

$$p = (\vec{p}, E) \quad \longrightarrow \quad (\vec{p}, |\vec{p}|) \qquad (p\text{-scheme}) \tag{11}$$

$$p = (\vec{p}, E) \quad \longrightarrow \quad (\hat{p}E, E) \qquad (E\text{-scheme}) \tag{12}$$

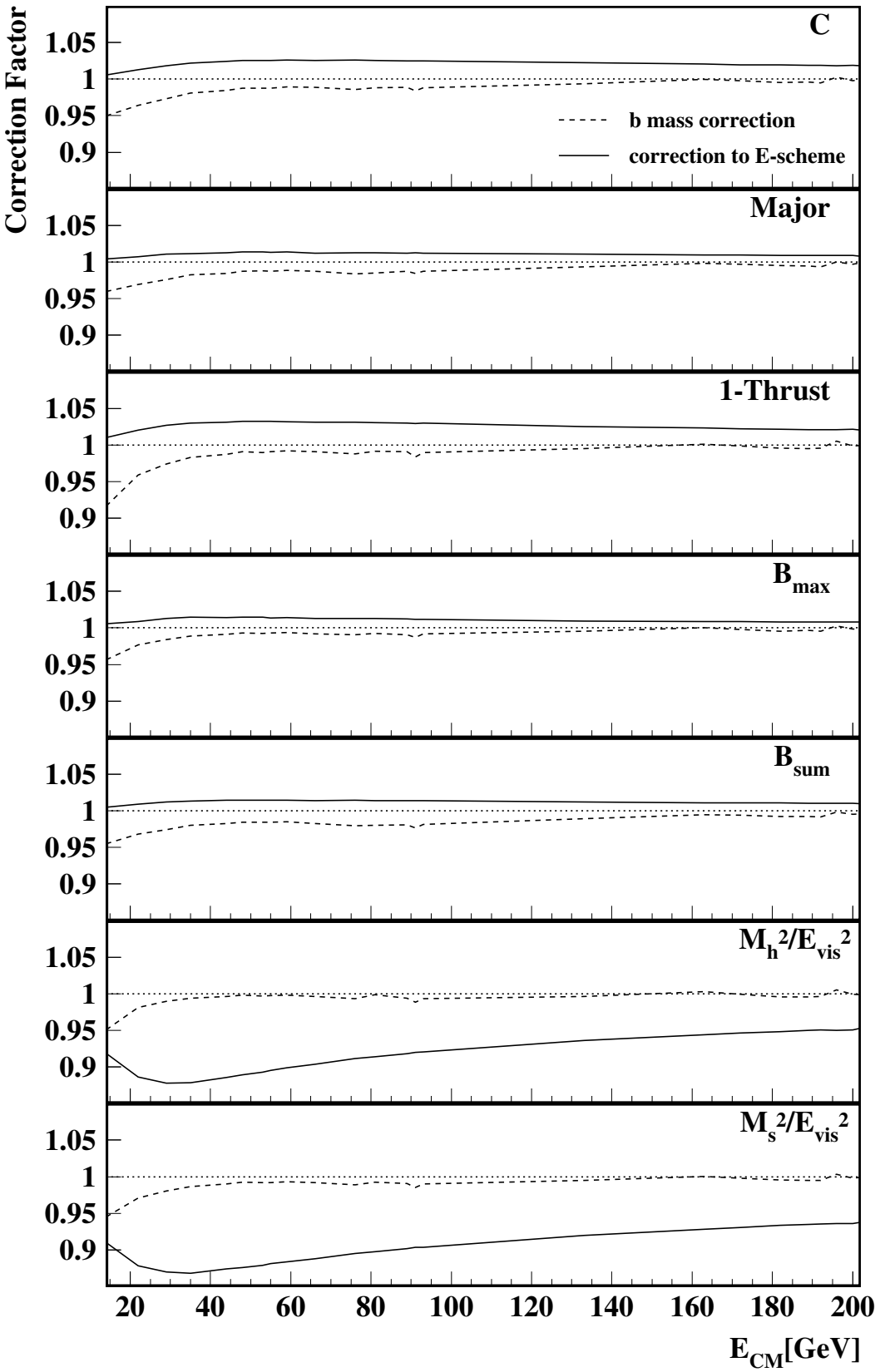

Figure 3: Corrections due to mass effects: The full line shows the relative change of the distribution of the observable due to a change into the E-scheme as a function of the energy. The dashed line shows the b–mass correction applied to the data.

with $\hat{p}$ being the unit vector in direction of $\vec{p}$.

The resulting observables have the same second order coefficients and the same power correction coefficient as standard definitions, because the theoretical calculations were performed for massless particles. Figure 3 shows, for shape observable means, the relative size of the corrections due to a change into the E-scheme as calculated by PYTHIA 6.1. $M_{\mathrm{h}}^2/E_{\mathrm{vis}}^2$ and $M_{\mathrm{s}}^2/E_{\mathrm{vis}}^2$ show the biggest changes (Other observables show in principle the same effect, but to a negligible extent.). As a consequence the E definitions of $M_{\mathrm{h}}^2/E_{\mathrm{vis}}^2$ and $M_{\mathrm{s}}^2/E_{\mathrm{vis}}^2$ are used wherever possible.

Besides the influence of final state hadron masses the influence of heavy b–hadron decays has to be taken into account. In order to correct for the kinematic effects of b–hadron decays, samples of 100000 b–quark and 100000 light quark events were simulated using PYTHIA 6.1. for each energy used. For the calculation of the shape observables all stable particles were considered. A correction was then calculated as the ratio of the event shape distribution (or mean) for light quark to b events considering the energy dependence of the fraction of b events in $\mathrm{e^+e^-}$annihilation. The correction is applied to the data throughout the analysis. It is shown for several event shape means in Figure 3. While the overall effect on the observables is of the order of a few % at the Z–peak, it rises well above 5% at low energy and influences the evolution of the observables.

2.4 Systematic uncertainties and definition of average values

In order to estimate systematic uncertainties of the corrected data distributions and of the quantities derived from them, the event selection and the correction procedure were varied. For each variation the analysis was repeated. The individual deviations from the central result were added in quadrature and considered as the systematic uncertainty.

The following variations were made in the event selection: the cut in the charged multiplicity was modified by ± 1 unit, the cut in the polar angle of the event Thrust axis was modified from 25° to 35°, and the cut on the observed visible energy was varied between 0.45 and 0.55. For the high energy data the $\sqrt{s'_{\mathrm{rec}}}$ cut was lowered to 0.8. For data at centre-of-mass energies above the WW threshold the weight of B_{min} in the cut relation was lowered to 480 from 500 and the WW cross–section was increased conservatively by 5%.

When hadronisation corrections are included in the analysis the predictions of ARIADNE were used instead of the standard choice PYTHIA. Model parameters are as given in [22]. Additionally $\pm 10\%$ was taken of the hadronisation correction as the systematic uncertainty. For the kinematically dominated b–hadron mass $\pm 20\%$ of the correction was taken as the systematic uncertainty.

For all renormalisation scale dependences the scale f was varied between half and twice the central value.

The fit results for the different observables are summarized by quoting two kinds of average values: the unweighted mean value with the R.M.S. as first error and the (error–)weighted mean value with the simple average of the individual statistical errors as the first error. The second error in both cases is the systematic uncertainty which has been propagated from the individual results. Quoting the R.M.S. indicates the size of theoretical uncertainties, while the average statistical error of the weighted mean value indicates the statistical significance of the results. Following from our definition, the statistical error of the weighted mean value is bigger than some individual statistical errors. A treatment of statistical correlation has not been performed, since our errors are dominantly systematic. Furthermore the statistical correlation between e.g. the event shape

means is high (≥ 0.8), thus the gain in reducing the statistical error would be negligible. Using these highly correlated observables is useful for other reasons: It provides a cross–check for QCD and indicates theoretical uncertainties, since their perturbative expansions show different properties (e.g. a different size of the second order contribution).

3 Comparison of experimental results to fragmentation models

Although among the oldest event shape measures, few data are available for the observable Major. Therefore in the Figures 4 and 5 the Major distributions are shown for several energies between 45 GeV and 202 GeV compared to predictions of the JETSET and ARIADNE Monte Carlo models. Except the lowest energy data at 45 GeV both simulations are almost indistinguishable. Data and simulation agree very well. The agreement between data and models is similarly good for other observables [31].

Figure 6 shows mean values in the energy range between 45 and 202 GeV for several observables, including the standard and the E definition of the Jet Masses. For comparison, results from JETSET simulations are shown. Again good agreement between data and model is observed. The dotted line in Figure 6 represents the shape observable mean at the parton level [1]. It is seen that the hadronisation correction, that is the difference between hadron and parton level curves is smallest for the observables $\langle \text{Major} \rangle$, $\langle M_{\text{h}}^2/E_{\text{vis}}^2 \rangle$, and $\langle B_{\text{max}} \rangle$. Also the slope of the parton and hadron level agrees best in these cases. On the other hand for the "subtracted" observables like $\langle \text{Oblateness} \rangle$, which have originally been constructed to compensate for hadronisation effects, show increased hadronisation corrections. In these cases the correction can have opposite sign to the other observables and sometimes even the sign of the slope of the energy evolution is opposite for parton and hadron level.

The behaviour of the hadronisation correction indicates a clear preference for observables such as $\langle \text{Major} \rangle$, $\langle M_{\text{h}}^2/E_{\text{vis}}^2 \rangle$, and $\langle B_{\text{max}} \rangle$ which are mainly sensitive to the hard gluon radiation in the events. It should, however, be noted that in these cases some technical problems may exist in the calculation of resummed theoretical predictions as soft gluon radiation may lead to a badly controlled exchange of the wide and narrow event hemispheres [30].

4 Power corrections to differential distributions

When comparing event shape data to perturbative calculations in general corrections for the effects of non-perturbative hadronisation are applied. One approach to hadronisation corrections is the renormalon induced power correction model proposed in [9]. In this model the origin of non–perturbative effects is determined by Borel transforming the observables and fixing the singularities found on the real axis. For several differential distributions and in the simplest approximation this results in shifting the distribution

[1] Parton and hadron level refer to the simulation of the hadronic final state. Parton level is before, hadron level after hadronisation has taken place.

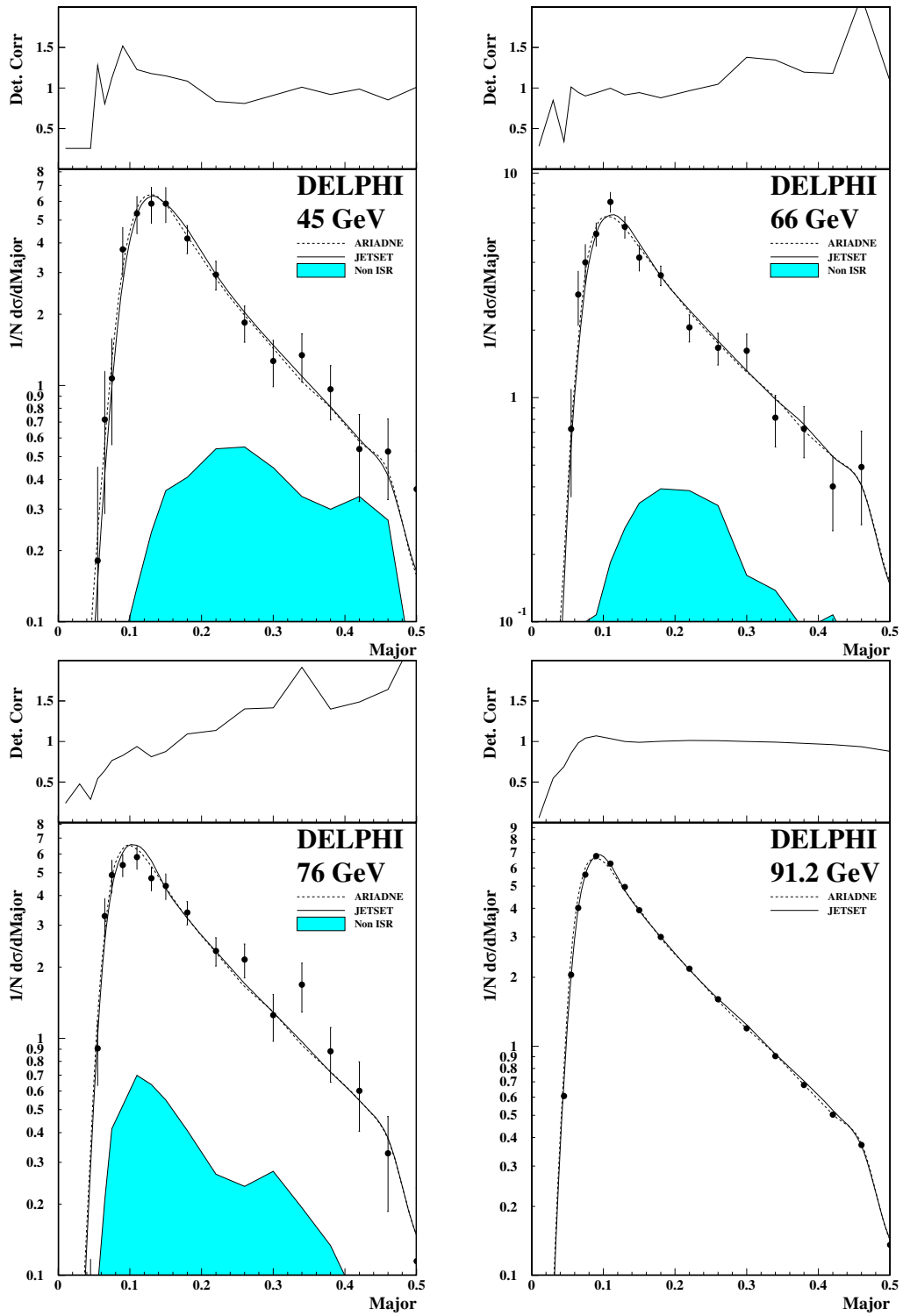

Figure 4: Distributions of the observable Major for centre-of-mass energies of 45, 66, 76 and 91.2 GeV compared to predictions of JETSET and ARIADNE. In each plot the upper chart shows the size of the detector correction, defined as $\frac{MC_{\mathrm{gen}}}{MC_{\mathrm{acc}}}$. The grey area indicates the distribution of non-radiative background events which has been subtracted.

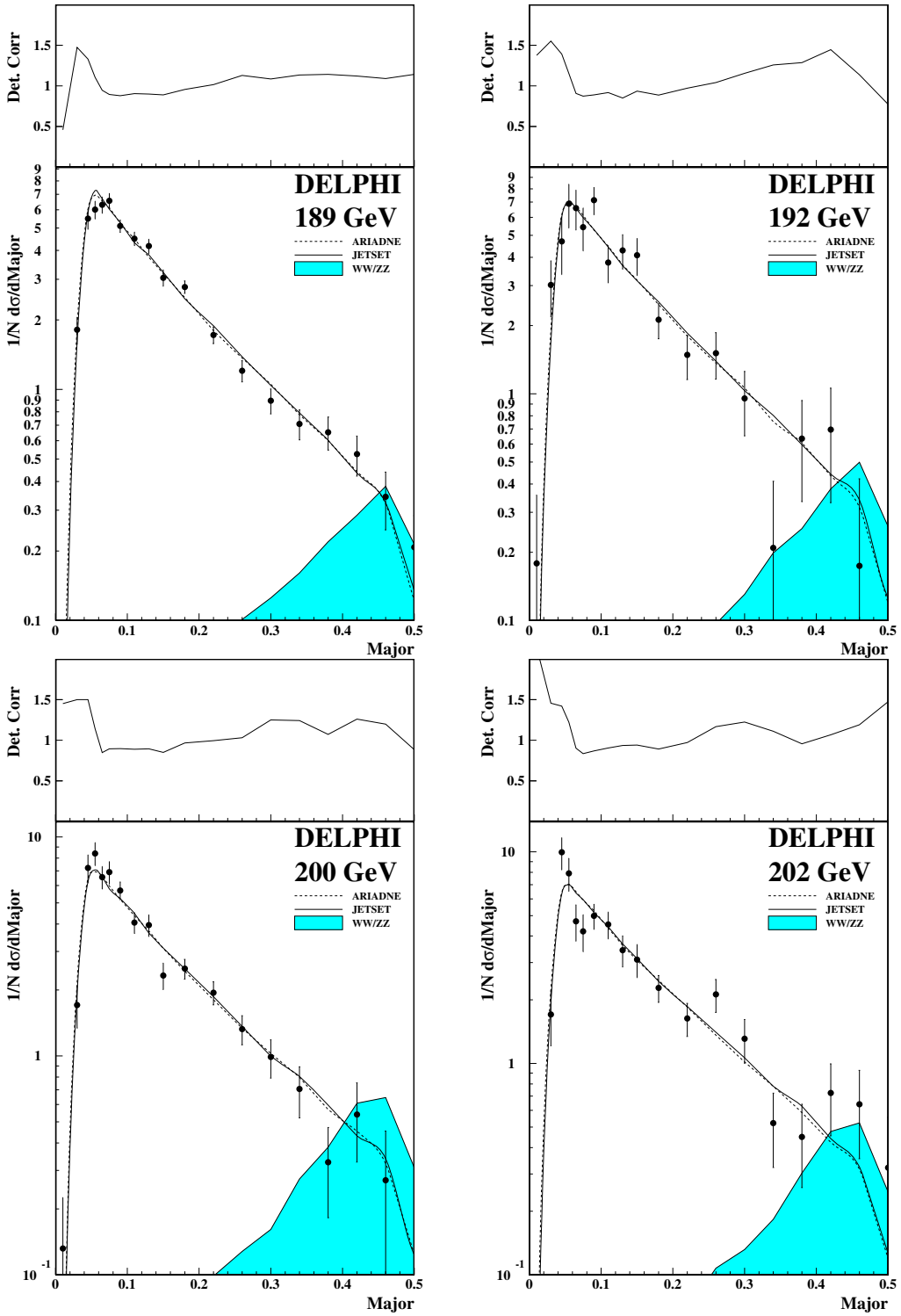

Figure 5: Distributions of the observable Major for centre-of-mass energies of 189, 192, 200 and 202 GeV compared to predictions of JETSET and ARIADNE. In each plot the upper chart shows the size of the detector correction, defined as $\frac{MC_{\mathrm{gen}}}{MC_{\mathrm{acc}}}$. The grey area indicates the distribution of WW and ZZ background events which has been subtracted.

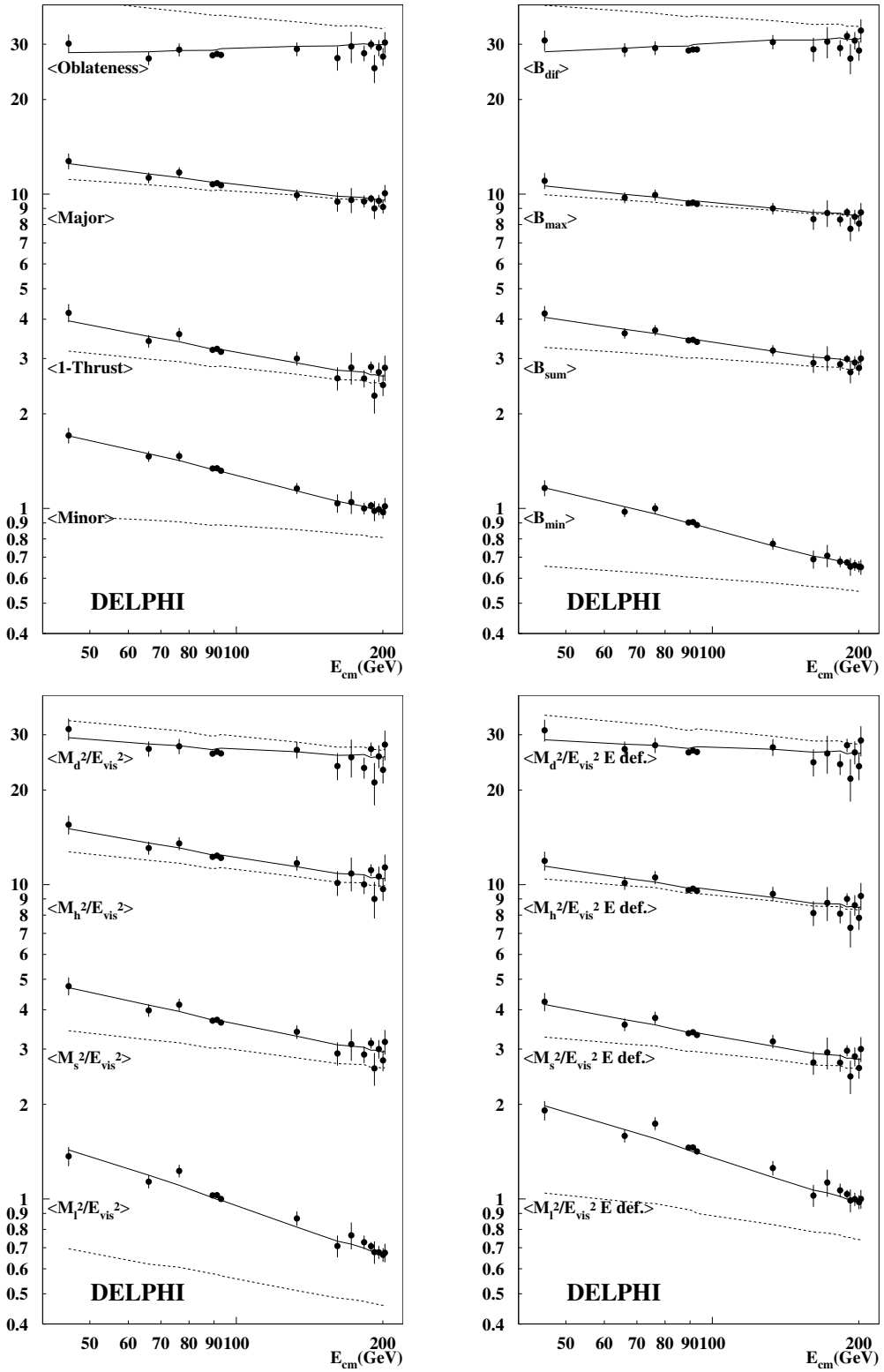

Figure 6: Event shape means for different observables in comparison to PYTHIA 6.1 predictions. The full line shows the hadron level, the dashed line the parton level.

$\mathcal{D}_f(f)$ of the observable f:

$$\begin{aligned}\mathcal{D}_f(f) &= \mathcal{D}_f^{pert}(f - \mathcal{P}\cdot c_f) \quad , \\ \mathcal{P} &= \frac{4C_F}{\pi^2}\mathcal{M}\frac{\mu_I}{E_{cm}}\left[\alpha_0(\mu_I) - \alpha_s(\mu) - \beta_0\frac{\alpha_s^2(\mu)}{2\pi}\left(\ln\frac{E_{cm}}{\mu_I} + \frac{K}{\beta_0} + 1\right)\right] \quad , \\ K &= (67/18 - \pi^2/6)C_A - 5n_{\rm f}/9 \quad .\end{aligned} \tag{13}$$

C_F and C_A are the QCD colour factors. α_0 is a non–perturbative parameter accounting for the contributions to the event shape below an infrared matching scale $\mu_{\rm I}$. The Milan factor $\mathcal{M}$ for three active flavours in the non–perturbative region is 1.49 [32].

Since the derivation of the coefficient c_f is based on resummation, there are only predictions for exponentiating observables available. c_f is an observable–dependent constant, which is identical to the coefficient in the predictions for event shape observable means. These are:

Observable	$1-$T	C	$M_{\rm h}^2/E_{\rm vis}^2$	$M_{\rm s}^2/E_{\rm vis}^2$
c_f	2	3π	1	2

In order to show all formulae in a coherent fashion, we use the definition of [1] for the coefficients of the β-function:

$$\beta_0 = \frac{33 - 2n_{\rm f}}{3} \quad , \qquad \beta_1 = \frac{153 - 19n_{\rm f}}{3} \quad , \qquad \beta_2 = 2857 - \frac{5033}{9}n_{\rm f} + \frac{325}{27}n_{\rm f}^2 \quad . \tag{14}$$

4.1 Power corrections for the Jet Broadenings $B_{\rm max}$ and $B_{\rm sum}$

Unlike the former observables, the Jet Broadenings cannot be sufficiently described by simple shifts, as the shift becomes a function of the Jet Broadening. Early predictions neglected the recoil of the quark due to the gluon emission, which proved to be an important effect. Improved calculations [33] take this mismatch into account. For the wide Jet Broadening $B_{\rm max}$ the correction coefficient has the form

$$c_{B_{\rm max}}(B_{\rm max}) = \frac{1}{2}\left(1/\ln B_{\rm max} + \eta_0 - 2 - \rho(\mathcal{R}') + \chi(\mathcal{R}') + \psi(1+\mathcal{R}') + \psi(1)\right) \quad , \tag{15}$$

where

$$\begin{aligned}\mathcal{R}' &= 2C_F\frac{\alpha_s(B_{\rm max}Q)}{\pi}(\ln B_{\rm max}^{-1} - \frac{3}{4}) \quad , & \eta_0 &= -0.6137 \quad , \\ \psi(z) &= \frac{d}{dz}\Gamma(z) \quad , & \rho(a) &= \int_0^1 dz\left(\frac{1+z}{2z\lambda(a)}\right)^{-a}\ln z(1+z) \quad , \\ \chi(a) &= \frac{2}{a}\left([\lambda(a)]^a - 1\right) \quad , & [\lambda(a)]^{-a} &\equiv \int_0^1 dz\left(\frac{1+z}{2z}\right)^{-a} \quad .\end{aligned}$$

For the total Jet Broadening $B_{\rm sum}$ the correction factor is

$$c_{B_{\rm sum}}(B_{\rm sum}) = \frac{1}{2}\left(2c_{B_{\rm max}}(B_{\rm sum}) + 2[\psi(1+2\mathcal{R}') - \psi(1+\mathcal{R}')] + H(\mathcal{B}^{-1})\right) \tag{16}$$

with

$$H(x) = \int_x^{z_0}\frac{dz}{z}\exp\{\mathcal{R}(x) - \mathcal{R}(z)\}\frac{\Gamma(1+2\mathcal{R}')}{\Gamma(1+2\mathcal{R}'+\mathcal{R}'(z))} \quad , \quad \mathcal{B} = \frac{2B_{\rm sum}}{e^{\gamma_E}\lambda(\mathcal{R}')} \quad ,$$

with $\gamma_E = 0.5772$ being the Euler constant and z_0 given by the position of the Landau Pole of the two loop radiator $\mathcal{R}$:

$$\mathcal{R}(x) = -\frac{4C_F}{\beta_0}\left[\left(\mathcal{L}-\frac{3}{4}\right)\ln\left(1-\frac{\ln x}{\mathcal{L}}\right)+\ln x\right] \quad , \qquad \mathcal{L} = \frac{2\pi}{\beta_0\alpha_s\left(1+K\frac{\alpha_s}{2\pi}\right)} \quad .$$

4.2 Power corrections for the Energy Energy Correlation EEC

The power corrections for the EEC have been calculated in [34]. Unlike for the other observables, there is no simple factorisation of the perturbative and non–perturbative components possible. Instead the non–perturbative coefficient is a part of the radiator function. The dominating non–perturbative part is based on the quark-gluon radiation and in the limit of large angles has a $Q^{-\gamma}$ like behaviour, with $\gamma \simeq 0.32$ for $n_{\rm f} = 5$. As a result one gets

$$\frac{d\Sigma}{d\cos\chi} = C(\alpha_s)\frac{(1+\tan^2\frac{\chi}{2})^3}{4}\frac{Q^2}{2}\int_0^\infty bdb\; J_0(bQ\tan\frac{\chi}{2})e^{-\mathcal{R}^{(PT)}(b)-\frac{1}{2}b^2\sigma}\gamma_E(1-2b\lambda) \quad , \tag{17}$$

where the perturbative radiator is defined by

$$\mathcal{R}^{(PT)}(b) = -\frac{16\pi C_F}{\beta_0^2}\cdot\left[\frac{1}{\alpha_s}(\ln(1-\ell)+\ell) - \frac{3\beta_0}{8\pi}\ln(1-\ell)+\frac{\beta_1}{2\pi\beta_0}\left(\frac{1}{2}\ln^2(1-\ell)+\frac{\ln(1-\ell)}{1-\ell}+\frac{\ell}{1-\ell}\right)\right] \quad ,$$

$$\ell = \beta_0\frac{\alpha_s}{2\pi}\ln\frac{bQe^{\gamma_E}}{2} \quad .$$

The linear non–perturbative correction $-2b\lambda$ stems from the correlation between quarks and soft gluons, where λ characterises the non–perturbative interaction at small momentum scales:

$$\lambda = \frac{4C_F}{\pi^2}\mathcal{M}\mu_I[\alpha_0(\mu_I)-\alpha_{0,0}^{PT}(\mu_I)] \quad . \tag{18}$$

The coefficient $C(\alpha_s)$ has the form

$$C(\alpha_s) = 1 - C_F\left(\frac{11}{2}+\frac{\pi^2}{3}\right)\frac{\alpha_s}{2\pi} \quad .$$

The radiator has its own non–perturbative component σ:

$$\sigma = \frac{C_F}{2\pi}\mu_I^2\left\{\left(\ln\frac{Q^2}{\mu_I^2}-\frac{1}{2}\right)[\alpha_1(\mu_I)-\alpha_{1,0}^{PT}(\mu_I)]+\alpha_{1,1}(\mu_I)-\alpha_{1,1}^{PT}(\mu_I)\right\} \quad . \tag{19}$$

The treatment of this non–perturbative component is unclear, as it is much weaker than the linear part and it is missing the quadratic part from the quark-gluon correlation. The $\alpha_{p,q}^{PT}(\mu_I)$ are normalisation factors:

$$\alpha_{p,q}^{PT}(\mu_I) = \alpha_s + \frac{\beta_0}{2\pi}\left(\ln\frac{Q}{\mu_I}+\frac{K}{\beta_0}+\frac{q+1}{p+1}\right)\alpha_s^2 \quad . \tag{20}$$

As a result one has to deal with three non–perturbative parameters: α_0, α_1 and $\alpha_{1,1}$, where α_0 is equivalent to the non–perturbative parameter of the other observables. A phenomenological prediction of α_1 is given in [34] from DIS experiments and the theoretical predictions are $\alpha_1 = 0.45$ and $\alpha_{1,1} = 0.55$. Since the formula for the EEC is a large angle approximation it is important to choose a proper fit region. Below 120° the prediction becomes invalid, while above 170° the influence of higher order logarithmic terms can no longer be neglected.

4.3 Comparison with data

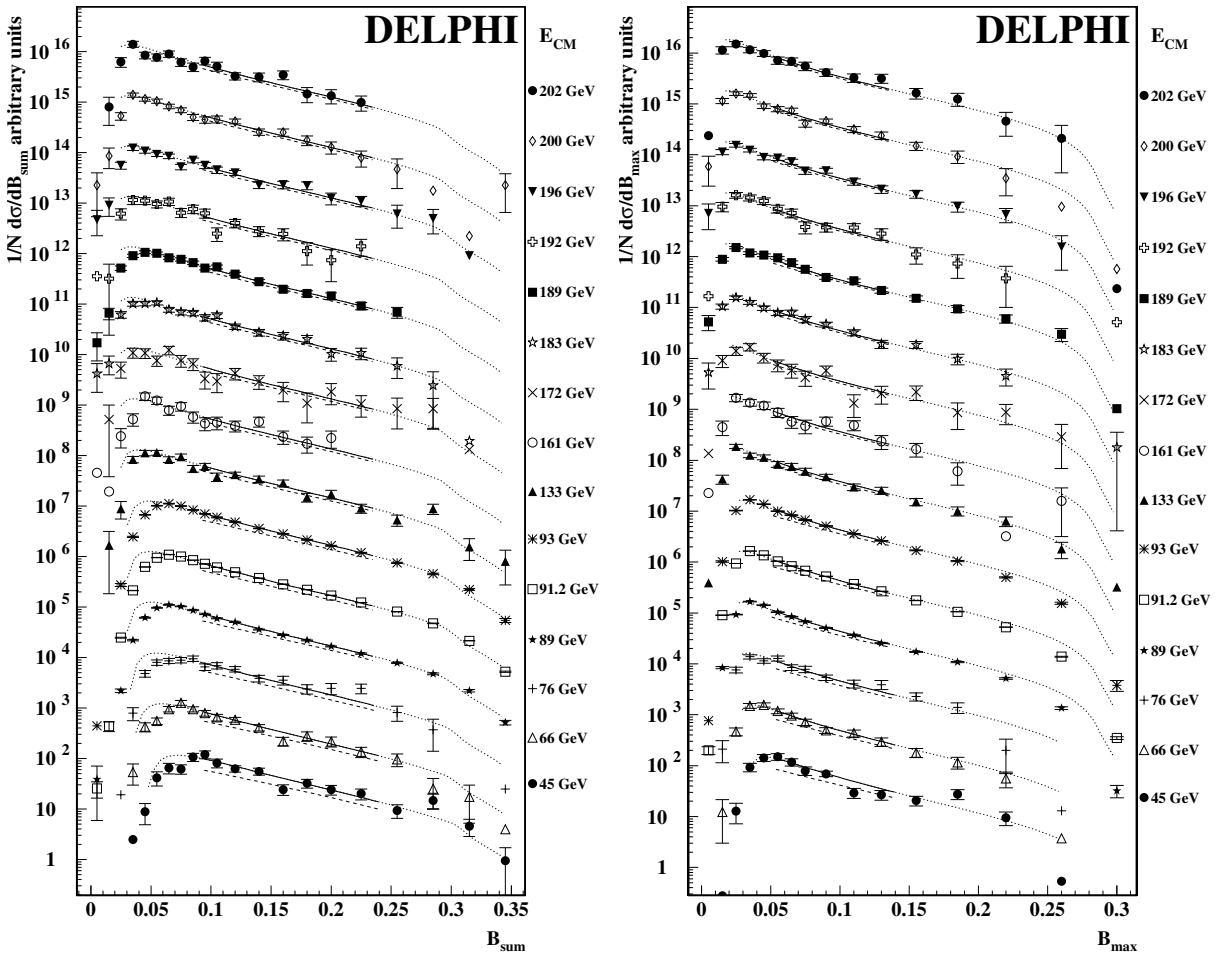

Figure 7: Jet Broadening distributions as measured by DELPHI for centre-of-mass energies between 45 and 202 GeV. The full line indicates the power model fit in the fit range, while the dotted line shows the extrapolation beyond the fit range. The dashed line shows the result after subtraction of the power correction.

The derivation of the power correction predictions in general relies on the resummation of logarithmically divergent terms. The validity of these predictions is thus limited to a kinematical region close to the two jet regime. This has been taken into account when choosing the fit intervals indicated in Table 3. Additionally it was required that the corrections applied to the data as well as the fit results obtained were stable. The experimental systematics have been determined as discussed in Section 2.4. In addition,

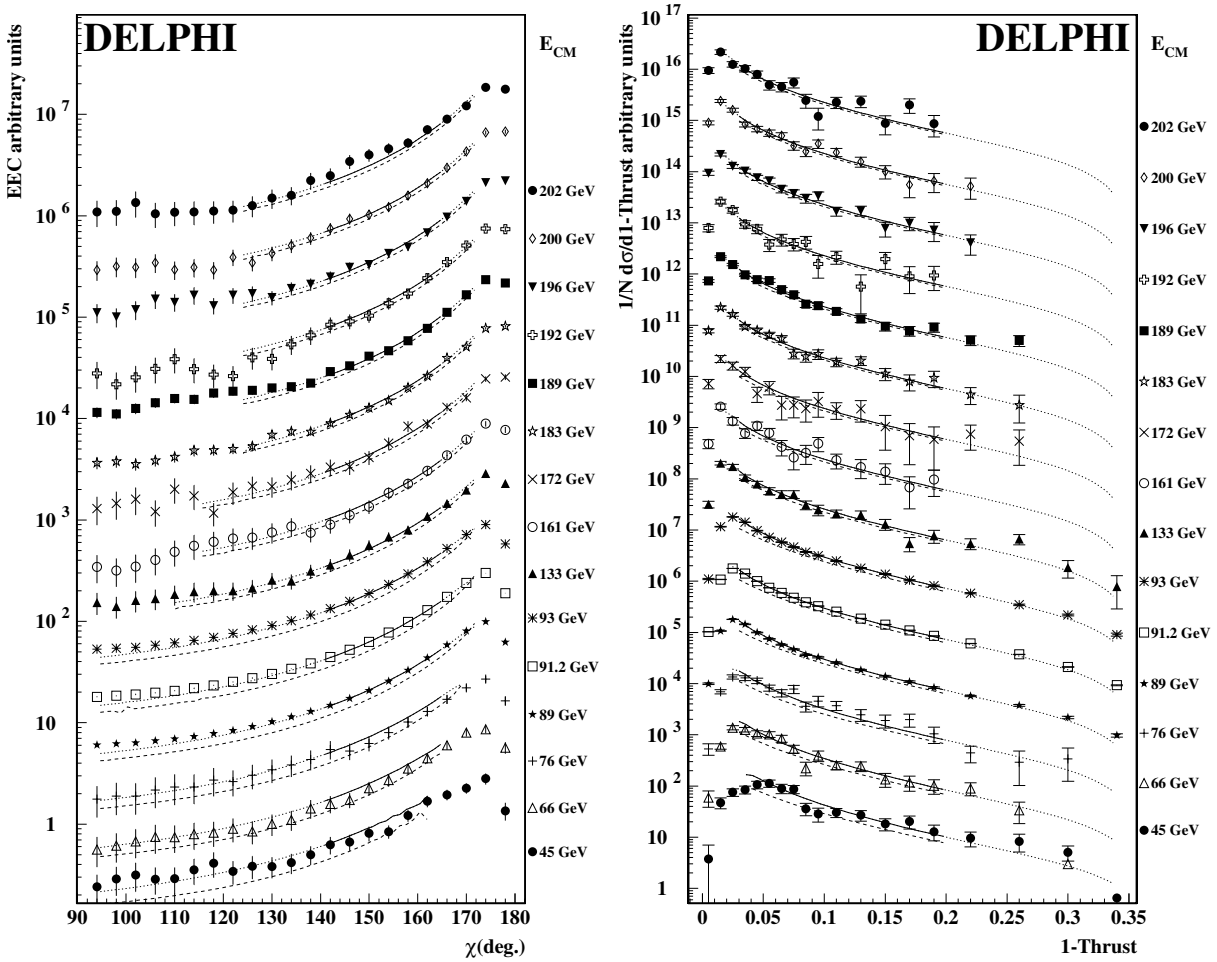

Figure 8: EEC and $1-$Thrust distributions as measured by DELPHI for centre-of-mass energies between 45 and 202 GeV. The full line indicates the power model fit in fit range, while the dotted line shows the extrapolation beyond the fit range. The dashed line shows the result after subtraction of the power correction.

changes of the fit ranges were applied as tabulated in Table 3. All systematic studies enter into the specified systematic uncertainty. Also the so called R matching was applied for the perturbative prediction instead of the standard logR matching [35]. It is notable that the change of the matching scheme has a significant influence on the size of the power corrections.

Examples of fits compared to the data on the Jet Broadenings, $1-$Thrust and the EEC, are shown in Figures 7 and 8. Results of the fitted parameters for all observables determined from DELPHI data are given in Table 4. The expected correlation of the fit parameters α_s and α_0 is displayed in Figure 9. The χ^2/ndf of the fit is acceptable when systematic uncertainties are included. The α_s values tend to be rather low compared to the world average value of $\alpha_s(M_{\mathrm{Z}}) = 0.1181 \pm 0.002$ [1] for most observables. The non–perturbative parameter α_0 is higher for the classical $M_{\mathrm{h}}^2/E_{\mathrm{vis}}^2$ as expected due to the influence of hadron mass effects. For the other observables the results for α_0 agree within a relative uncertainty of about 20%.

The result of the fit of the EEC is shown in Figure 8 (left). The influence of the non–perturbative parameters α_1 and $\alpha_{1,1}$ is found to be much smaller than the influence of α_0.

Observable	lower	upper
$1-T$	0.03 (0.02)	0.2 (0.24)
B_{max}	0.05 (0.04)	0.14 (0.16)
B_{sum}	0.09 (0.08)	0.17 (0.19)
$M^2_{\mathrm{h}}/E^2_{\mathrm{vis}}$	0.03 (0.02)	0.12 (0.14)
$M^2_{\mathrm{hE}}/E^2_{\mathrm{vis}}$	0.03 (0.02)	0.12 (0.14)
$M^2_{\mathrm{hp}}/E^2_{\mathrm{vis}}$	0.03 (0.02)	0.12 (0.14)
$M^2_{\mathrm{s}}/E^2_{\mathrm{vis}}$	0.03 (0.02)	0.12 (0.14)
$M^2_{\mathrm{sE}}/E^2_{\mathrm{vis}}$	0.03 (0.02)	0.12 (0.14)
$M^2_{\mathrm{sp}}/E^2_{\mathrm{vis}}$	0.03 (0.02)	0.12 (0.14)
C-parameter	0.2 (0.16)	0.68 (0.72)

Table 3: Fit intervals used for the fit of power corrections to event shape distributions. The variations of the fit interval used for systematic studies are shown in brackets.

The precision of the experimental data is insufficient to determine $\alpha_{1,1}$. A three parameter fit neglecting $\alpha_{1,1}$ yielded: $\alpha_s = 0.1173 \pm 0.0021 \pm 0.0008$, $\alpha_0 = 0.478 \pm 0.046 \pm 0.017$ and $\alpha_1 = 0.005 \pm 0.026 \pm 0.025$ with a $\chi^2/ndf = 52.7/90$. Since this fit indicates that the non–perturbative part of the radiator α_1 can be neglected, an additional two parameter fit was performed, resulting in: $\alpha_s = 0.1171 \pm 0.0018 \pm 0.0004$, $\alpha_0 = 0.483 \pm 0.040 \pm 0.011$, with $\chi^2/ndf = 53/91$. The α_0 value for the EEC is consistent with the values determined from the other observables (see Table 4).

4.4 Measurement of the non–perturbative shift from the Sudakov Shoulder

So far all predictions apply near to the two jet region. For some observables, however, the predictions seem to hold even in the far three jet region. In order to provide evidence for this observation the three jet limit of several observables was studied.

Despite the fact that QCD event shape observables are constructed so as to be infrared- and collinear safe, there can still be infinities at accessible points in phase space. The finiteness is only restored after the resummation of divergent terms to all orders. The resulting structure is called a Sudakov shoulder [36]. The most common case is the phase space boundary of the three jet region, which introduces a visible edge into the distributions. The position can be calculated and is, for example, 2/3 for 1-Thrust and 3/4 for the C-parameter. A simple inspection of the distributions and the corresponding model curves shows that the shoulder is typically shifted to higher values, and that power corrections describe the shift rather well.

The shift for the C parameter can be measured by fitting the slope of the logarithmic distribution on both sides of the shoulder. The intersection of these fits is a good approximation to the shoulder position. The result of the fit can be seen in Figure 10, the fitted position of the shoulder is at C$= 0.794 \pm 0.016_{stat} \pm 0.001_{sys}$ corresponding to a shift of $+0.044 \pm 0.016_{stat} \pm 0.001_{sys}$ with respect to the nominal position. Using a value of $c_{\mathrm{C}} = 3\pi$ for the C parameter, a value of $\alpha_0 = 0.476 \pm 0.097_{stat} \pm 0.0015_{sys}$ is obtained from Equation 13. This result is well consistent with the result obtained from the fit of

Observable	$\alpha_s(M_Z)$	$\alpha_0(\mu_I = 2\,\mathrm{GeV})$	χ^2/ndf
$1-T$	0.1154±0.0002±0.0017 +0.0004	0.543±0.002±0.014 +0.013	291/180
$B_{\max}$	0.1009±0.0003±0.0016 −0.0018	0.571±0.005±0.031 +0.021	106/90
B_{sum}	0.1139±0.0006±0.0015 −0.0035	0.465±0.005±0.013 +0.008	88/75
$M^2_{\mathrm{h}}/E^2_{\mathrm{vis}}$	0.1076±0.0001±0.0013 +0.0003	0.872±0.000±0.026 +0.005	158/90
$M^2_{\mathrm{hE}}/E^2_{\mathrm{vis}}$	0.1056±0.0003±0.0006 +0.0001	0.692±0.007±0.010 +0.010	120/90
$M^2_{\mathrm{hp}}/E^2_{\mathrm{vis}}$	0.1055±0.0004±0.0010 +0.0001	0.615±0.009±0.022 +0.010	130/90
$M^2_{\mathrm{s}}/E^2_{\mathrm{vis}}$	0.1190±0.0004±0.0030 +0.0001	0.734±0.004±0.034 +0.009	66/45
$M^2_{\mathrm{sE}}/E^2_{\mathrm{vis}}$	0.1166±0.0004±0.0028 +0.0002	0.583±0.004±0.027 +0.007	60/45
$M^2_{\mathrm{sp}}/E^2_{\mathrm{vis}}$	0.1156±0.0005±0.0010 +0.0001	0.536±0.005±0.010 +0.008	54/45
C-Parameter	0.1097±0.0004±0.0032 −0.0008	0.502±0.005±0.047 +0.021	191/180
weighted mean	0.1078±0.0005±0.0013 −0.0012	0.546±0.005±0.022 +0.013	
unweighted mean	0.1110±0.0055±0.0007 −0.0008	0.559±0.073±0.009 +0.013	
EEC	0.1171±0.0018±0.0004	0.483±0.040±0.011	53/90

Table 4: Determination of α_s and α_0 from a fit to event shape distributions. Only DELPHI measurements are included in the fit. The first error is the statistical uncertainty from the fit, the second one is the systematic uncertainty, the third the difference with respect to the R matching scheme. Only E–definition Jet Masses have been taken for the means. For the definition of the mean values see section 2.4.

the overall distribution $\alpha_0 = 0.502 \pm 0.005_{stat} \pm 0.047_{sys}$ suggesting a constant shift over the whole three jet region in the case of the C parameter.

5 Power corrections in event shape means

The mean values of event shape variables are defined as:

$$\langle f \rangle \quad = \quad \frac{1}{\sigma_{\mathrm{tot}}} \int f \frac{df}{d\sigma} d\sigma \quad = \quad \frac{1}{N_{\mathrm{evt.}}} \sum_{i=1}^{N_{\mathrm{evt.}}} f_i \quad .$$

We have calculated them from the detector corrected and binned distributions. Hence they are fully inclusive quantities depending on a single energy scale only, and are well suited for low statistics analyses as the statistical uncertainty is minimised by using all events. Though the characteristics of the event shape observables may differ in specific regions of the value of the observable, global properties can be assessed from the energy dependence of the mean value.

5.1 The Dokshitzer and Webber ansatz

The analytical power ansatz [12,37] including the Milan factor [10,11] is used to determine α_s from mean event shapes. This ansatz provides an additive non–perturbative term $\langle f_{\mathrm{pow}} \rangle$ to the perturbative $\mathcal{O}(\alpha_s^2)$ QCD prediction $\langle f_{\mathrm{pert}} \rangle$,

$$\langle f \rangle = \langle f_{\mathrm{pert}} \rangle + \langle f_{\mathrm{pow}} \rangle \quad , \tag{21}$$

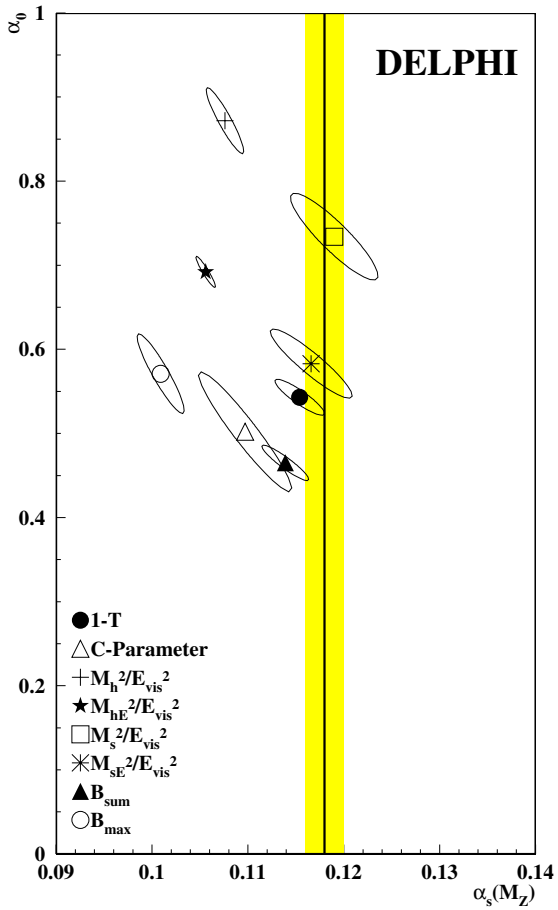

Figure 9: Results of the fits to shape distributions in the α_s–α_0 plane. The band indicates the world average of α_s.

where the 2nd order perturbative prediction can be written as

$$\langle f_{\mathrm{pert}} \rangle = A\frac{\alpha_s(\mu)}{2\pi} + \left(A \cdot \beta_0 \ln\frac{\mu}{E_{cm}} + B\right)\left(\frac{\alpha_s(\mu)}{2\pi}\right)^2, \tag{22}$$

A and B are known coefficients [38–40] and μ is the renormalisation scale. The power correction is given by

$$\langle f_{\mathrm{pow}} \rangle = c_f \mathcal{P} \quad , \tag{23}$$

where $\mathcal{P}$ is as defined in Equation 13.

The observable-dependent coefficient c_f is identical for shapes and means. In the case of the jet broadenings c_f cannot be described as a constant. Here the non–perturbative contribution is proportional to $1/(Q\sqrt{\alpha_s(Q)})$ [33]:

$$c_f = c_{\mathrm{B}}\left(\frac{\pi\sqrt{c_{\mathrm{B}}}}{2\sqrt{C_F\alpha_{\overline{MS}}\left(1+K\frac{\alpha_{\overline{MS}}}{2\pi}\right)}} + \frac{3}{4} - \frac{\beta_0 c_{\mathrm{B}}}{6C_F} + \eta_0\right) \quad , \tag{24}$$

where c_{B} is 1/2 in the case of $\langle B_{\mathrm{max}} \rangle$ and 1 for $\langle B_{\mathrm{sum}} \rangle$, $\eta_0 = -0.6137056$.

In the following analysis the infrared matching scale μ_{I} was set to 2 GeV, as suggested in [12], and the renormalisation scale μ was set to E_{cm}.

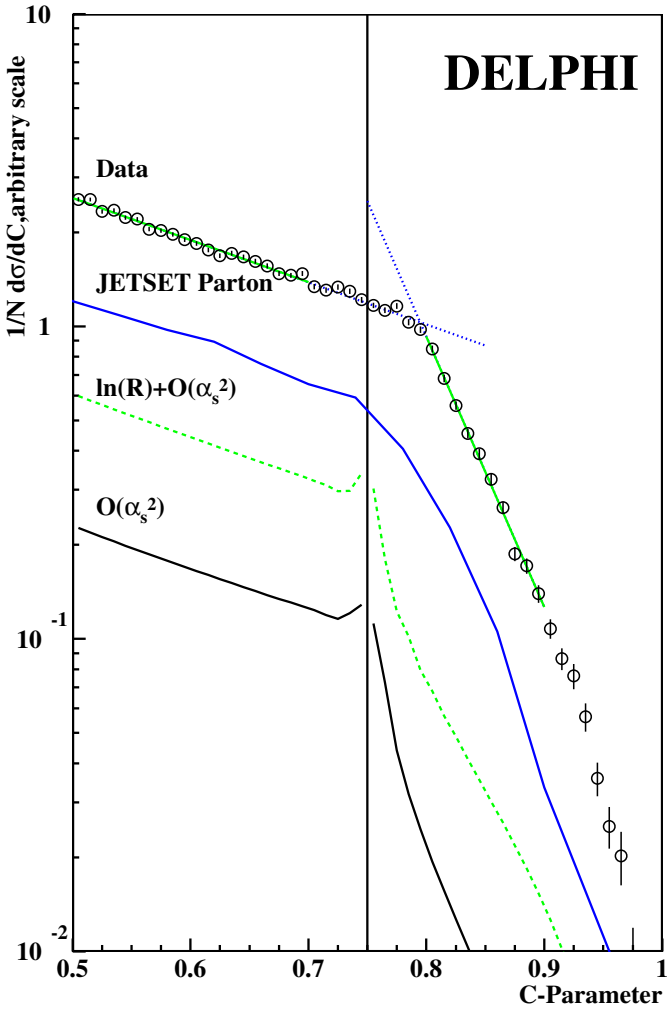

Figure 10: Determination of the shift of the Sudakov shoulder in comparison to predictions. The vertical positions are arbitrarily scaled. The fit range (straight line) and the extrapolation to the intersection point (dotted line) are shown. The vertical line denotes the three jet limit of 0.75 .

A combined fit of α_s and α_0 to a large set of measurements[2] at different energies [41] has been performed. In the χ^2 calculation, statistical and systematic uncertainties were considered. For $E_{\rm cm} \geq M_{\rm Z}$, only DELPHI measurements were included in the fit. Figure 11 (left) shows the measured mean values of $\langle 1-T \rangle$, $\langle M^2_{\rm hE}/E^2_{\rm vis} \rangle$ (standard– and E definition), $\langle C \rangle$, $\langle B_{\rm max} \rangle$ and $\langle B_{\rm sum} \rangle$ as a function of the centre-of-mass energy together with the results of the fit. The fit values of α_s and α_0 are summarised in Table 5 and displayed in the α_s–α_0 plane in Figure 11 (right). The systematic uncertainty was obtained as described in Section 2.4. In addition $\mu_{\rm I}$ was varied from 1 GeV to 3 GeV. Both uncertainties were added in quadrature.

The α_s values obtained from these fits are consistent with each other and in good agreement with the world average $\alpha_s(M_{\rm Z}) = 0.118 \pm 0.002$ [1]. The extracted α_0 values are around 0.5 as expected in [11,37]. However, the predicted universality (e.g. the observable independence) is satisfied on a 25% level only. This problem remains even though only the Jet Mass in the E–definition, $\langle M^2_{\rm hE}/E^2_{\rm vis} \rangle$, is considered which avoids

[2] We concentrated on up–to–date results.

Observable	$\alpha_0(\mu_I = 2\,\mathrm{GeV})$	$\alpha_s(M_Z)$	χ^2/ndf
$\langle 1-T\rangle$	0.491±0.016±0.009	0.1241±0.0015±0.0031	26.5/41
⟨C-Parameter⟩	0.444±0.020±0.008	0.1222±0.0020±0.0030	11.6/23
$\langle M_{\mathrm{h}}^2/E_{\mathrm{vis}}^2\rangle$	0.601±0.058±0.012	0.1177±0.0030±0.0018	14.1/27
$\langle M_{\mathrm{hp}}^2/E_{\mathrm{vis}}^2\rangle$	0.300±0.222±0.127	0.1185±0.0104±0.0057	10.1/15
$\langle M_{\mathrm{hE}}^2/E_{\mathrm{vis}}^2\rangle$	0.339±0.229±0.129	0.1197±0.0107±0.0058	9.5/15
$\langle M_{\mathrm{s}}^2/E_{\mathrm{vis}}^2\rangle$	0.544±0.160±0.093	0.1335±0.0118±0.0074	7.2/15
$\langle M_{\mathrm{sp}}^2/E_{\mathrm{vis}}^2\rangle$	0.378±0.138±0.084	0.1288±0.0104±0.0067	8.7/15
$\langle M_{\mathrm{sE}}^2/E_{\mathrm{vis}}^2\rangle$	0.409±0.143±0.086	0.1304±0.0107±0.0069	8.2/15
$\langle B_{\mathrm{max}}\rangle$	0.438±0.041±0.027	0.1167±0.0018±0.0007	10.1/23
$\langle B_{\mathrm{sum}}\rangle$	0.463±0.032±0.009	0.1174±0.0021±0.0020	8.8/23
weighted mean	0.468±0.080±0.008	0.1207±0.0048±0.0026	
unweighted mean	0.431±0.048±0.039	0.1217±0.0046±0.0030	

Table 5: Determination of α_0 and α_s from a fit to a large set of event shape mean values measured from different experiments [41]. For $E_{\mathrm{cm}} \geq M_{\mathrm{Z}}$ only DELPHI measurements are included in the fit. The first error is the statistical uncertainty from the fit, the second one is the systematic uncertainty. For the mean values only the E–definition Jet Masses have been used. For the definition of the mean values see section 2.4.

a strong additional energy dependence due to the influence of hadron masses. The α_s values are higher and the α_0 values are lower than the corresponding results from event shape distributions (compare Figures 9 and 11).

5.2 Simple power corrections

Power corrections in the Dokshitzer–Webber framework can only be calculated for the set of exponentiating observables. The experimental evidence for corrections which show $1/Q$ behaviour is however not restricted to this type of observables. The tube model indicates the existence of power corrections on simple phase space assumptions.

In order to determine approximate power corrections for all observables measured the "simple power correction" ansatz is used. Here an additional power term $\langle f_{pow}\rangle = C_1/Q$ is added to the $\mathcal{O}(\alpha_s^2)$ perturbative expansion of the observable, with C_1 being an observable dependent, unknown constant. The disadvantage of this simple ansatz is that a double counting in the infrared region of the observables is not corrected for as in the Dokshitzer–Webber approach.

Two different types of fits were performed to the DELPHI data using this simple model. Firstly, in order to investigate whether this simple model yields sensible values for α_s at all, both parameters, $\Lambda_{\overline{MS}}$ and C_1, were left free in the fit. The results obtained are given in Table 6. The average value of these α_s results and the corresponding R.M.S. obtained only from the fully inclusive observables are $\alpha_s = 0.1250 \pm 0.0058$ for the unweighted mean and $\alpha_s = 0.1250 \pm 0.0054$ for the weighted mean. The reasonable values for α_s as well as the acceptable χ^2/ndf of 6/7 of the averaging support the approximate validity of this simple power correction model. Secondly, in order to get comparable estimates of the size of the power correction for the different observables, $\Lambda_{\overline{MS}} = 0.250\,\mathrm{GeV}$ was chosen,

Observable	C_1	$\alpha_s(M_Z)$	χ^2/ndf
$\langle 1-T\rangle$	0.483±0.085±0.048	0.1312±0.0019±0.0032	26.3/41
$\langle$Major$\rangle$	0.405±0.979±0.595	0.1166±0.0071±0.0043	9.8/15
$\langle$C-Parameter$\rangle$	2.242±0.469±0.249	0.1278±0.0024±0.0032	11.0/23
$\langle M_{\rm h}^2/E_{\rm vis}^2\rangle$	0.502±0.119±0.027	0.1210±0.0033±0.0018	15.1/27
$\langle M_{\rm s}^2/E_{\rm vis}^2\rangle$	0.736±0.689±0.408	0.1375±0.0132±0.0081	7.1/15
$\langle M_{\rm hE}^2/E_{\rm vis}^2\rangle$	0.130±0.434±0.246	0.1215±0.0113±0.0061	9.3/15
$\langle M_{\rm sE}^2/E_{\rm vis}^2\rangle$	0.341±0.617±0.373	0.1342±0.0119±0.0075	8.1/15
$\langle B_{\rm max}\rangle$	0.241±0.075±0.018	0.1203±0.0016±0.0009	9.2/23
$\langle B_{\rm sum}\rangle$	0.593±0.159±0.050	0.1236±0.0018±0.0022	7.8/23
$\langle {\rm EEC}_{70^\circ-110^\circ}\rangle$	0.285±0.637±0.541	0.1307±0.0102±0.0088	18.8/15
$\langle {\rm EEC}_{30^\circ-150^\circ}\rangle$	0.022±0.470±0.691	0.1395±0.0051±0.0082	41.2/15
$\langle {\rm JCEF}_{110^\circ-160^\circ}\rangle$	0.011±0.676±0.954	0.1201±0.0049±0.0070	31.4/15
weighted mean		0.1250±0.0054±0.0024	
unweighted mean		0.1250±0.0058±0.0032	

Table 6: Determination of C_1 and α_s from a fit to a large set of measurements of different experiments [41]. For $E_{\rm cm} \geq M_{\rm Z}$ only DELPHI measurements are included in the fit. The first quoted error is the uncertainty from the fit, the second one is the systematic uncertainty. In calculating the mean values, the Jet masses using standard definitions, EEC and JCEF have been omitted. For the definition of the mean values see section 2.4.

Observable	C_1
$\langle 1-T\rangle$	1.093±0.016±0.289
$\langle$Major$\rangle$	0.390±0.020±0.170
$\langle$C-Parameter$\rangle$	4.330±0.063±0.713
$\langle M_{\rm h}^2/E_{\rm vis}^2\rangle$	0.649±0.023±0.076
$\langle M_{\rm s}^2/E_{\rm vis}^2\rangle$	1.839±0.051±0.136
$\langle M_{\rm hE}^2/E_{\rm vis}^2\rangle$	0.327±0.018±0.072
$\langle M_{\rm sE}^2/E_{\rm vis}^2\rangle$	1.265±0.033±0.136
$\langle B_{\rm max}\rangle$	0.406±0.008±0.046
$\langle B_{\rm sum}\rangle$	1.199±0.012±0.190
$\langle {\rm EEC}_{70^\circ-110^\circ}\rangle$	1.177±0.021±0.163
$\langle {\rm EEC}_{30^\circ-150^\circ}\rangle$	2.066±0.015±0.227
$\langle {\rm JCEF}_{110^\circ-160^\circ}\rangle$	0.484±0.026±0.223

Table 7: Determination of C_1 with a fixed $\Lambda_{\overline{MS}} = 0.250$ GeV from a fit to a set of measurements of different experiments [41]. For $E_{\rm cm} \geq M_{\rm Z}$ only DELPHI measurements are included in the fit. The first uncertainty is the uncertainty from the fit, the second one is the systematic uncertainty. For the definition of the mean values see section 2.4.

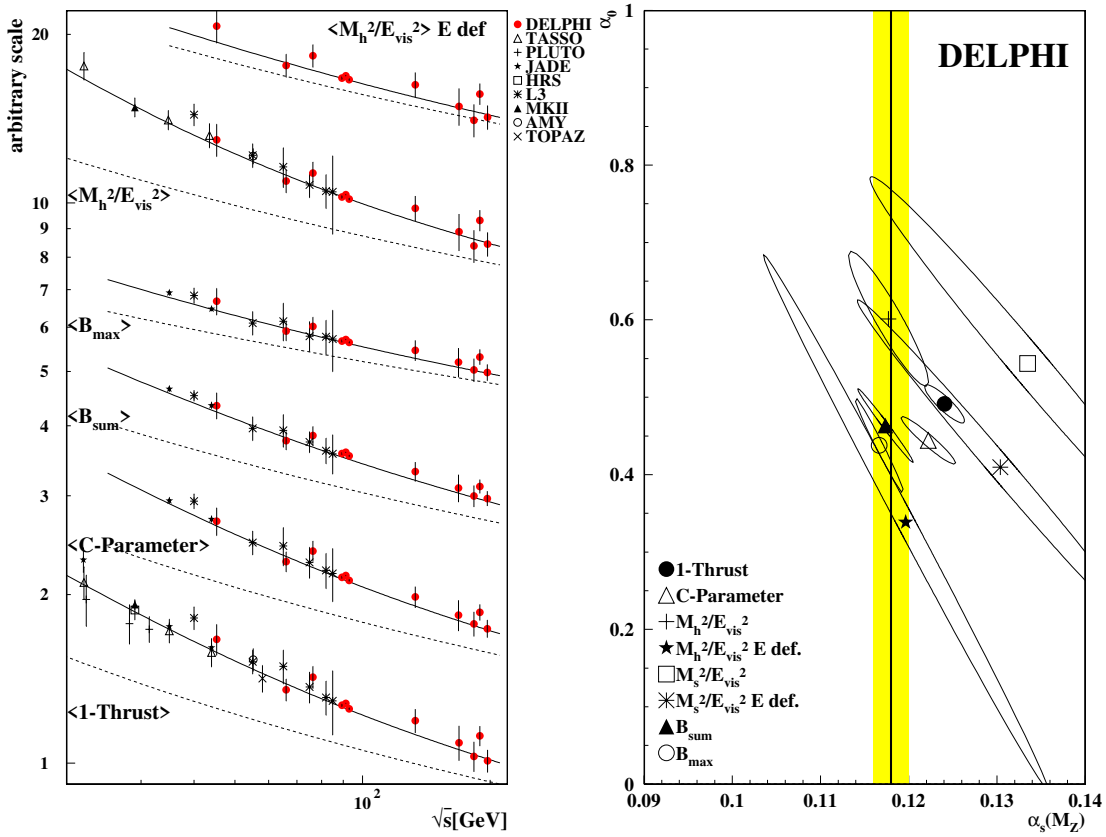

Figure 11: Left: Measured mean values of $\langle 1-T\rangle$, $\langle M_{\mathrm{h}}^2/E_{\mathrm{vis}}^2\rangle$, $\langle C\rangle$, $\langle B_{\mathrm{sum}}\rangle$ and $\langle B_{\mathrm{max}}\rangle$ as a function of the centre-of-mass energy. For clarity some of the high energy data have been merged. The solid lines present the results of the fits with Equations (21–23), the dotted lines show the perturbative part only. Right: Results of the Dokshitzer-Webber fits in the α_s–α_0 plane. The band indicates the world average of α_s.

leaving only C_1 as a free parameter. The fitted values of C_1 are contained in Table 7, where the total experimental uncertainty for C_1 is given.

The ratio of the power model parameter normalised to the first order perturbative coefficient, C_1/A, is plotted against the ratio of second to first order perturbative coefficient B/A in Figure 14. The normalisation to A is made in order to make the observables directly comparable. Experimentally a clear correlation between the genuine non–perturbative parameter C_1 and the purely perturbative parameter B is observed. This strong correlation indicates that the term C_1/Q should not be interpreted as purely non–perturbative.

6 Interpretation of event shape means using RGI perturbation theory

Today the $\overline{MS}$ scheme is commonly used for the representation of perturbative calculations of physical observables. In consequence predictions for power corrections have

also been given in this scheme. Nonetheless the $\overline{MS}$ scheme is only one of an infinite set of equally well suited schemes.

A previous DELPHI analysis using experimentally optimised scales for the determination of α_s from event shape distributions [42] has shown that the experimentally optimised scales of different observables are correlated with the corresponding effective charge, ECH [43], or principle of minimal sensitivity, PMS [44], scales. The renormalisation group invariant (RGI) approach [5,7] uses the same central equations as the method of effective charge [43], however the motivation and philosophy differ. The derivation of the RGI method makes no reference to any renormalisation scheme whatsoever. In the following sections the RGI predictions [5,45,46] for fully inclusive shape observable means are explored.

6.1 Theoretical background of RGI

Instead of expanding an observable R into a perturbative series in $\alpha_s(Q)$, the starting point of the RGI method is a β-function like expansion of $\frac{dR}{dQ}$ in R:

$$Q\frac{dR}{dQ} = -bR^2(1+\rho_1 R+\rho_2 R^2+\dots) = b\rho(R) \quad . \tag{25}$$

Note that here $R = 2\langle f\rangle/A$ is normalised such that the perturbative expansion in α_s/π begins with unit coefficient. It can be shown [5,43], that the coefficients ρ_i are scheme invariant and that the scale dependence cancels out completely. The ρ_i can be calculated from the coefficients r_1, r_2 of the perturbative expansion:

$$\rho_1 = c_1 \quad , \qquad\qquad \rho_2 = c_2 + r_2 - r_1 c_1 - r_1^2 \quad , \tag{26}$$

$$b = \frac{\beta_0}{2} \quad , \quad c_1 = \frac{\beta_1}{2\beta_0} \quad , \quad c_2 = \frac{\beta_2}{32\beta_0} \quad , \quad r_1 = \frac{B}{2A} \quad , \quad r_2 = \frac{C}{4A} \quad .$$

The coefficients A and B are defined in Equation 22, C is the corresponding third order coefficient.

The solution of Equation 25 is equivalent to the well known implicit equation for α_s:

$$b\ln\frac{Q}{\Lambda_R} = \frac{1}{R} - \rho_1 \ln\left(1+\frac{1}{\rho_1 R}\right) + \int_0^R dx\left(\frac{1}{\rho(x)} + \frac{1}{x^2(1+\rho_1 x)}\right) \quad . \tag{27}$$

Here Λ_R is an R-specific scale parameter. In next-to-leading (NLO) order α_s the integrand vanishes and the solution of this equation is identical to a scale which sets the NLO contribution of the perturbative series to zero. Using the so called Celmaster Gonzalves equation [47], Λ_R can be converted into $\Lambda_{\overline{MS}}$ without any loss of precision:

$$\frac{\Lambda_R}{\Lambda_{\overline{MS}}} = e^{r_1/b}\left(\frac{2c_1}{b}\right)^{-c_1/b} \quad . \tag{28}$$

In a study of event shape observables a test of the validity of RGI perturbation theory is currently limited to NLO. It should therefore be verified that higher order corrections are small and that the NLO β-function (e.g. the inclusion up to the ρ_1 term in Equation 25) is a sufficient approximation. A check on higher order contributions is implied by a consistency check of the α_s values measured from different observables.

It is important to note that the above derivation only holds for observables that depend on one single energy scale, such as fully inclusive observables. Selections or cuts in the

observable introduce additional scales that have to be included into equation 25. Thus it is not to be expected that the aforementioned simple form of RGI is valid, say, for y_{cut} dependent jet rates or bins of event shape distributions. The application of the RGI method to ranges of the EEC or JCEF as performed in the following sections is thus not fully justified, except by the success of the comparison to data. The RGI method may also to some extent apply here as the intervals chosen are rather wide and represent an important fraction of the events. Moreover it should be noted that the total integrals over the EEC or JCEF are normalised to 2 or 1, respectively. RGI can also not be unambiguously calculated for observables like $M_d^2 = M_h^2 - M_l^2$, as $M_l^2 = \min(\mathrm{M}_+^2, \mathrm{M}_-^2)$ is only known to leading order.

It is possible to include power corrections into RGI. In [45] it is shown that the existence of non–perturbative corrections leads to a predictable asymptotic behaviour of the renormalisation group equation. This can be included into the equation as a modification of the ρ function [48]:

$$\rho(x) \rightarrow \rho(x) - \frac{K_0}{b} x^{-c_1/b} e^{-1/bx} \quad , \tag{29}$$

where K_0 is a free, unknown parameter that determines the size of the non–perturbative correction. The correction is approximately equal to a simple C_1/Q power correction in the $\overline{MS}$ scheme with [48]:

$$C_1 = -K_0 \cdot e^{r_1/b} \cdot \left(\frac{b}{2}\right)^{c_1/b} \cdot \Lambda_{\overline{MS}} \quad . \tag{30}$$

As RGI pertubation theory and the ECH method are based on the same basic equation, the choice of the ECH renormalisation scheme is implicit in RGI perturbation theory. Therefore it may be controversial whether measurements of α_s performed using RGI are renormalisation scale or scheme independent. However, with respect to the β function (e.g. its leading coefficients, β_0 and β_1) the situation is different. Their measurement based on Equation 25 is free of any scheme ambiguity since this relation holds in *any* renormalisation scheme. Moreover β_0 and β_1 are renormalisation scheme invariant quantities. Dhar and Gupta summarize their discussion with the following words:"(...) we have shown that in a renormalizable massless field theory with a single dimensionless coupling constant, *only* the derivative $\rho(R)$ of a physical quantity R with respect to an external scale is well defined and unambiguously calculable"[5].

6.2 Comparing RGI with power corrections to data

Using the same data as in the case of simple power corrections, a combined fit of Λ_{R} and K_0 is performed to the RGI with power correction theory using Equation 29. A correction is applied for the influence of the b–mass but not for further hadronisation effects. RGI plus power correction describes the behaviour of the data well for all observables considered including EEC and JCEF and leads to a consistent result for α_s. The fit results are given in Table 8 and Figure 12. The uncertainties for the jet masses in E–definition, Major as well as for JCEF and EEC are large as no data from low energy experiments are available in these cases. The result for $\langle 1 - \mathrm{T} \rangle$ agrees reasonably with the comparable analysis presented in [48]. Note that in [48] no b–mass correction was applied. Small differences are understood as being due to the b–mass correction and the differing choice of input data. Combining the α_s results for the fully inclusive observables yields $\alpha_s = 0.1179 \pm 0.0020 \pm 0.0013$ for the unweighted mean and $\alpha_s = 0.1184 \pm 0.0031 \pm 0.0035$

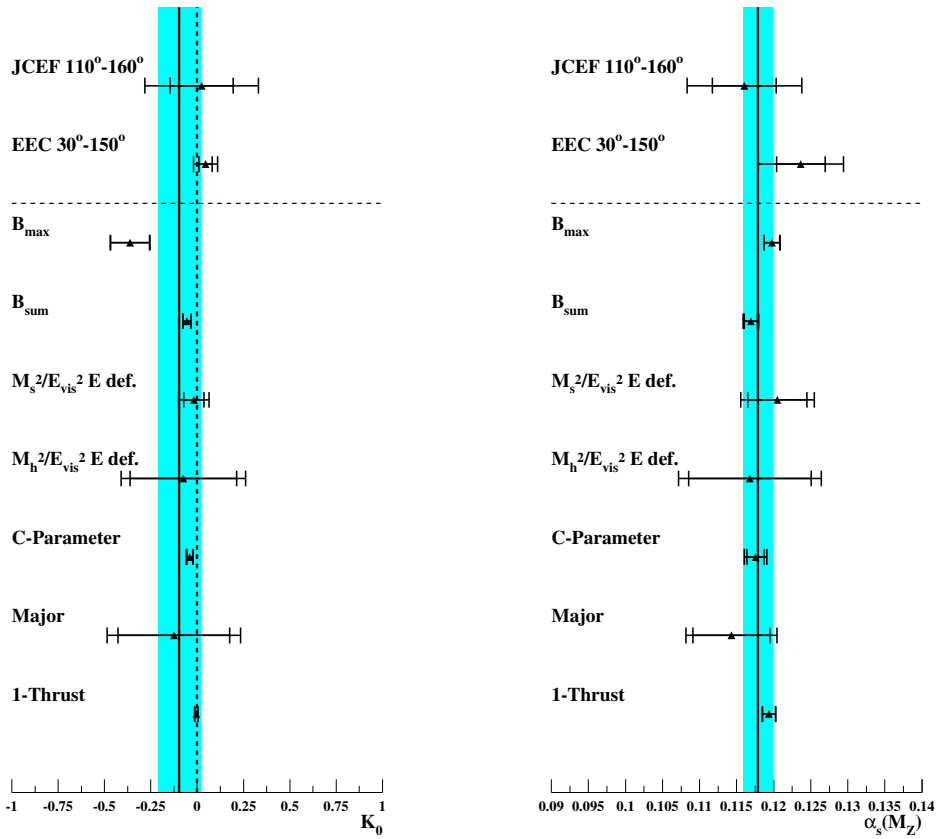

Figure 12: Results for a combined fit of Λ_R and the power correction parameter K_0 using Equation 29. Left: The results for the non–perturbative parameter K_0. Right: The results for $\alpha_{\mathrm{s}}(M_{\mathrm{Z}})$ deduced from Λ_{R}. The straight line shows the unweighted mean, the shaded band the R.M.S. obtained from the fully inclusive observables only.

for the weighted mean with a χ^2/ndf of 7.0/5. The spread of the α_s results from the fit of RGI with power corrections is only half of the size as for the simple power correction case.

The fact that the results for K_0 are small (most are compatible with zero) is surprising. The smallness of the K_0 results in combination with the consistent α_s values from all 9 different observables casts doubt on the interpretation of the measured $\langle f_{pow} \rangle$ contribution (see Equation 21) as a genuine non–perturbative term. In view of the observed consistency one is led to presume a better approximation of the data by RGI perturbation theory and the $\overline{MS}$ scheme appears as an unfortunate choice. This conjecture implies that the power terms measured for shape observable means in the previous section mainly parameterise terms which can in principle be calculated perturbatively.

To elucidate this conjecture further, Thrust is taken as example. Here for a fixed α_s=0.118, $C_1/Q = (1.108 \pm 0.017)\,\mathrm{GeV}/Q$ is found as the simple power correction in the $\overline{MS}$ scheme. Using Equation 30 this translates into $K_0 = -0.32 \pm 0.006$. In the RGI plus power term approach $K_0 = -0.005 \pm 0.008$ is observed, however. Contrary to the simple power model or the ansatz of Equation 23, here the power contribution is insignificant. From the influence of hadron masses, a small kinematical dependence similar to an inverse power law is to be expected. However, the absolute size of this mass correction cannot yet be safely calculated [30].

Observable	K_0	$\alpha_s(M_Z)$	χ^2/ndf
$\langle 1-T\rangle$	$-0.005\pm0.008\pm0.003$	$0.1194\pm0.0009\pm0.0003$	31.0/39
$\langle$Major$\rangle$	$-0.126\pm0.302\pm0.197$	$0.1143\pm0.0052\pm0.0033$	9.8/13
$\langle$C-Parameter$\rangle$	$-0.040\pm0.016\pm0.009$	$0.1175\pm0.0012\pm0.0010$	11.0/21
$\langle M_h^2/E_{vis}^2\rangle$	$-0.112\pm0.028\pm0.006$	$0.1219\pm0.0014\pm0.0005$	19.6/25
$\langle M_s^2/E_{vis}^2\rangle$	$-0.034\pm0.072\pm0.038$	$0.1249\pm0.0065\pm0.0035$	7.1/13
$\langle M_{hE}^2/E_{vis}^2\rangle$	$-0.074\pm0.288\pm0.172$	$0.1168\pm0.0083\pm0.0050$	9.3/13
$\langle M_{sE}^2/E_{vis}^2\rangle$	$-0.018\pm0.054\pm0.061$	$0.1205\pm0.0040\pm0.0029$	11.0/13
$\langle B_{max}\rangle$	$-0.362\pm0.105\pm0.021$	$0.1198\pm0.0010\pm0.0005$	8.8/21
$\langle B_{sum}\rangle$	$-0.055\pm0.022\pm0.004$	$0.1169\pm0.0009\pm0.0005$	7.7/21
$\langle \mathrm{EEC}_{70^\circ-110^\circ}\rangle$	$0.008\pm0.095\pm0.075$	$0.1174\pm0.0065\pm0.0051$	18.8/13
$\langle \mathrm{EEC}_{30^\circ-150^\circ}\rangle$	$0.045\pm0.036\pm0.054$	$0.1236\pm0.0033\pm0.0047$	40.8/13
$\langle \mathrm{JCEF}_{110^\circ-160^\circ}\rangle$	$0.024\pm0.171\pm0.254$	$0.1160\pm0.0043\pm0.0064$	31.4/13
weighted mean	$-0.018\pm0.114\pm0.068$	$0.1184\pm0.0031\pm0.0035$	
unweighted mean	$-0.097\pm0.114\pm0.057$	$0.1179\pm0.0020\pm0.0013$	

Table 8: Results for a RGI plus non–perturbative parameter fit to a large set of measurements of different experiments [41]. For $E_{\mathrm{cm}} \geq M_{\mathrm{Z}}$ only DELPHI measurements are included in the fit. The first uncertainty is the statistical uncertainty from the fit, the second one is the systematic uncertainty. For the mean values only the E–definition Jet Masses have been used and both EEC and JCEF have been omitted. For the definition of the mean values see section 2.4.

6.3 Comparing pure RGI to data

In light of the negligible power term ($\propto K_0$) observed in the previous section, a comparison of the data and the pure RGI perturbation theory appears interesting. No hadronisation correction is included and Λ_{R} is the only free parameter of the theory. This implies that Λ_R can be precisely determined from each individual shape observable mean measurement allowing for stringent tests of RGI by comparing the energy dependence of individual observables or by comparing the $\Lambda_{\overline{MS}}$ or $\alpha_s(M_Z)$ values obtained from different observables. Note that these parameters can be deduced from Λ_{R} without loss of precision (see Equation 28).

Observed deviations between different energy points of an observable should mainly be due to hadronisation or mass corrections. From the above section these corrections are already known to be small ($\simeq$ few %). Differences in α_s values between different observables represent different power corrections as well as missing higher order terms of RGI perturbation theory. Clearly the α_s value for each observable will be dominated by the precise measurements at the Z pole.

Figure 13 compares the energy dependence of the fully inclusive event shape means considered in this analysis to the RGI prediction. The data shown are the same as explained in the simple power correction section. The energy dependence of all observables is well represented by RGI theory. The χ^2/ndf of the fits is acceptable for all observables (see Table 9) and similar to the RGI plus power correction case. The observed values of α_s of the different observables agree reasonably well, with the exception of the standard definition of $M_{\mathrm{h}}^2/E_{\mathrm{vis}}^2$ or $M_{\mathrm{s}}^2/E_{\mathrm{vis}}^2$ (not shown here). For these observables mass terms are known to be important and reflect into higher α_s values compared to the results using the E-scheme.

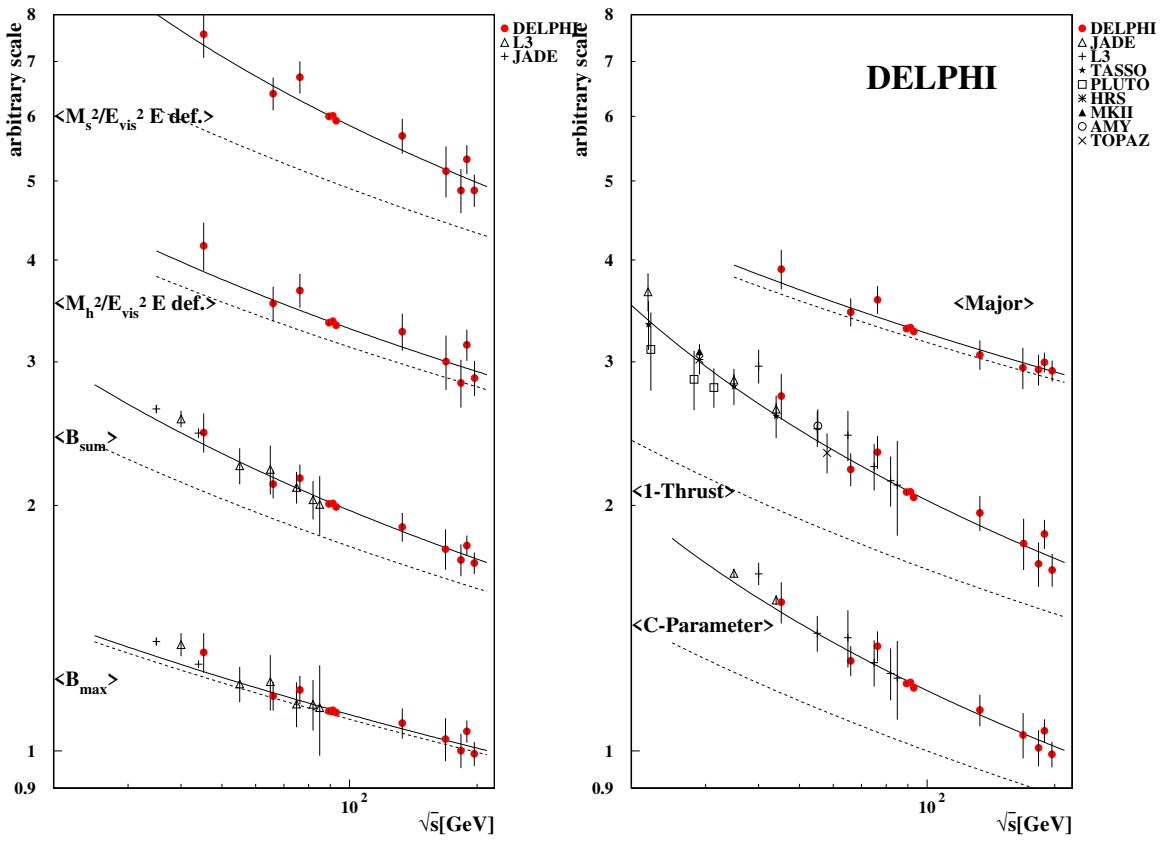

Figure 13: Comparison of the data on event shape means with the prediction of pure RGI perturbation theory (full line). For clarity some of the high energy data have been merged. The dashed line represents the $\overline{MS}$ expectation with the same $\alpha_s(M_Z)$.

The RGI α_s results for the different observables are also shown in Figure 15 compared to results of RGI with power corrections and α_s values obtained in $\overline{MS}$ with simple power corrections as well as with Monte Carlo hadronisation corrections. The last have been calculated as usual by comparing the hadron and parton level result in a Monte Carlo fragmentation model (Pythia). It is evident that RGI leads to a far better consistency between different observables than the simple power corrections or the Monte Carlo hadronisation corrections. In comparison to the RGI plus power correction ansatz the spread of the α_s values is not significantly increased. The unweighted mean and R.M.S. spread of the α_s values from the fully inclusive means shown in Figure 15 is $\alpha_s = 0.1201 \pm 0.0020$, using the weighted mean yields $\alpha_s = 0.1195 \pm 0.0002$. The average from pure RGI is still consistent with that using the RGI plus power correction ansatz. The overall α_s shift of about 2% at Z energies indicates a possible influence of power terms. The spread of the unweighted mean α_s values is only of the order of 0.002. It indicates possible differences in power terms and uncalculated higher order contributions which are naively expected to be of the order $\alpha_s^3 \sim 0.002$. The strongly differing second order contributions (compare the B/A values of the different observables in $\overline{MS}$ shown in Figure 14) as well as the differing NLLA expansions suggest differing higher order terms for the individual observables.

Observable	$\alpha_s(M_Z)$	χ^2/ndf
$\langle 1-T\rangle$	0.1199±0.0002±0.0002	31.9/40
$\langle$Major$\rangle$	0.1166±0.0001±0.0003	10.1/14
$\langle$C-Parameter$\rangle$	0.1205±0.0002±0.0002	24.6/22
$\langle M_{\rm h}^2/E_{\rm vis}^2\rangle$	0.1274±0.0005±0.0017	46.9/26
$\langle M_{\rm s}^2/E_{\rm vis}^2\rangle$	0.1282±0.0006±0.0005	7.6/14
$\langle M_{\rm hE}^2/E_{\rm vis}^2\rangle$	0.1189±0.0004±0.0005	9.4/14
$\langle M_{\rm sE}^2/E_{\rm vis}^2\rangle$	0.1216±0.0004±0.0004	8.1/14
$\langle B_{\rm max}\rangle$	0.1236±0.0002±0.0004	32.6/22
$\langle B_{\rm sum}\rangle$	0.1194±0.0001±0.0004	21.5/22
$\langle {\rm EEC}_{70^\circ-110^\circ}\rangle$	0.1169±0.0002±0.0001	18.8/14
$\langle {\rm EEC}_{30^\circ-150^\circ}\rangle$	0.1199±0.0001±0.0001	44.0/14
$\langle {\rm JCEF}_{110^\circ-160^\circ}\rangle$	0.1155±0.0002±0.0001	31.5/14
weighted mean	0.1195±0.0002±0.0010	
unweighted mean	0.1201±0.0020±0.0003	

Table 9: Results for a pure RGI fit to a large set of measurements of different experiments [41]. For $E_{\rm cm} \geq M_{\rm Z}$ only DELPHI measurements are included in the fit. The first error is the statistical uncertainty from the fit, the second one is the systematic uncertainty. For the mean values only the E–definition Jet Masses have been used and both EEC and JCEF have been omitted. For the definition of the mean values see section 2.4.

As a further illustration of the validity of RGI one may try to calculate the size of the power terms observed in the $\overline{MS}$ analysis. The power term can be approximated as the difference of the RGI and the $\overline{MS}$ terms:

$$\frac{C_1}{E_{cm}} = R_{\rm RGI}(E_{cm}) - R_{\overline{\rm MS}}(E_{cm}) \tag{31}$$

for a fixed $\Lambda_{\overline{MS}} = 250\,{\rm MeV}$. This value corresponds to the average α_s as obtained from the RGI analysis. As this ansatz is slightly energy dependent, M_Z has been chosen as the reference energy. Figure 14 shows the comparison between the measured simple power correction terms and the calculated power term using pure RGI. The strong correlation between C_1/A and B/A for fully inclusive means (left side) is well represented by the above ansatz. It also holds reasonably well for the JCEF and the EEC. Here the ratio of the first and second order coefficient B/A can be adjusted by an appropriate choice of the χ integral.

The agreement of the measured values C_1/A and the RGI curve depends on the choice of $\Lambda_{\overline{MS}}$. A higher value of 280 MeV as indicated by the upper edge of the grey band shown in Figure 14 requires the data points to move down about by the same amount, leading to a difference between the data and the curve of about the width of the grey band.

Similarly to the simple power term C_1, the α_0 values of the Dokshitzer-Webber model can be calculated and obviously agree reasonably with the fitted values, as shown in Figure 16. The measured α_0 values, show a scatter around a universal value anticipated by the Dokshitzer Webber model. Even this scatter is described reasonably by the RGI prediction.

Finally a remark on the connection of RGI to optimised scales is in order here. Though reference [5] stresses the difference in philosophy of RGI perturbation theory and scale optimisation there is an obvious connection.

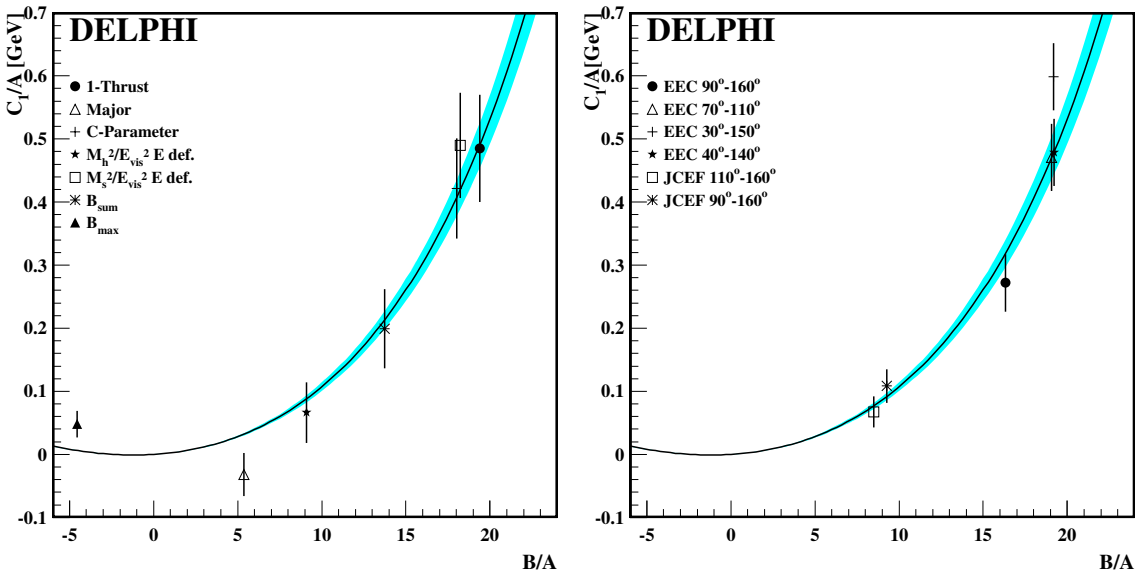

Figure 14: Comparison of the results for C_1/A obtained from a fit with fixed $\Lambda_{\overline{MS}} = 0.250\,\mathrm{GeV}$ and the prediction from pure RGI. The shaded band shows the variation of $\Lambda_{\overline{MS}}$ between 0.220 GeVand 0.280 GeV. Left: fully inclusive observables. Right: different integration intervals of EEC and JCEF. Note that the data points are correlated.

RGI perturbation theory describes the data on fully inclusive shape means well without any renormalisation scale dependence whatsoever. This implies that a fit of the renormalisation scale using the standard $\mathcal{O}(\alpha_s^2)$ expansion leads to a scale value where the scale dependence of the $\mathcal{O}(\alpha_s^2)$ prediction vanishes. This is the PMS scale which is close to the ECH scale. The above contiguity has been observed numerically [31] and found to be valid within errors.

6.4 Measuring the QCD β-function based on the RGI analysis

Although RGI perturbation theory is based on the RGE the β-function itself is not fixed by the RGI approach. As the β-function for an observable R and the QCD coupling is identical in second order this implies that the β-function, or rather the coefficients β_0 and ρ_1, can be directly inferred from the energy evolution of the event shape observable means (see Equation 27). As ρ_1 induces only a small correction ($\mathcal{O}(4\%)$) and cannot be simultaneously determined with β_0 given the current precision of the data, it has been fixed to the QCD expectation. Assuming QCD, the number of active flavours, n_f, can be determined as an alternative to determining β_0. In these cases β_0 and ρ_1 were calculated from the QCD relations using the fitted n_f and assuming $N_\mathrm{C} = C_\mathrm{A} = 3$.

The approach allows β_0 to be measured under the assumption that QCD is valid. In order to compare the result with predictions from e.g. super symmetric extensions of the standard model one of course cannot rely on the QCD calculation for β_1. Instead one needs to fit the full energy dependence. This analysis is described in section 6.5.

The implicit Equation 27 can be fitted to data on shape observable means leaving Λ_R and β_0 (or n_f) as free parameters. Note that this fit is independent of an n_f dependence entering implicitly through the second order perturbative coefficient B. This holds as the offset term $\beta_0 \ln \Lambda_R$ is unrestricted because Λ_R is a fit parameter and implies that a real measurement of β_0 or n_f can be performed.

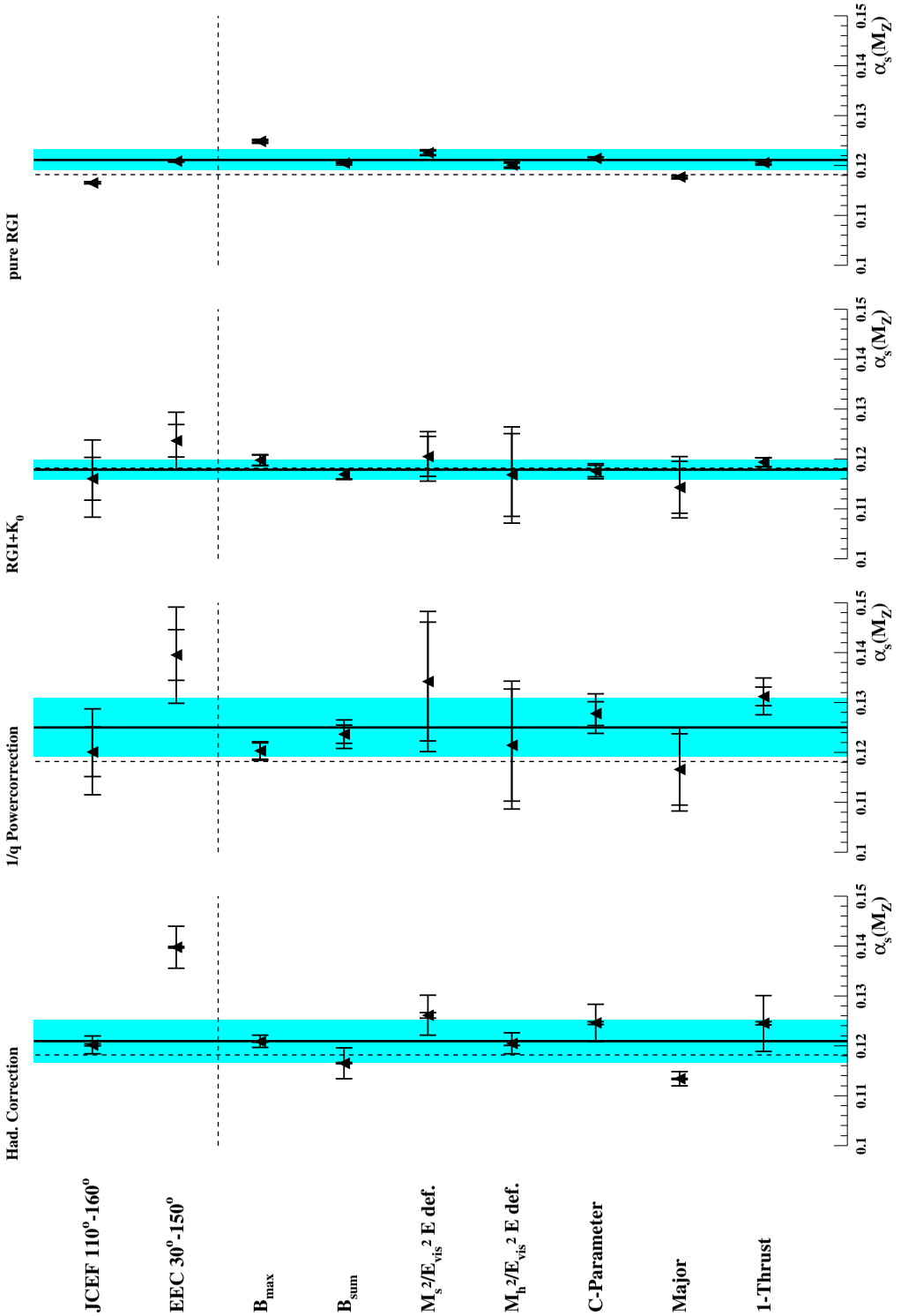

Figure 15: Results for α_s for different observables and methods. The straight line shows the unweighted mean, the shaded bar the variance for the fully inclusive observables. As a reference the world average value of $\alpha_s(M_Z) = 0.1181 \pm 0.002$ [1] is shown as dashed line.

Observable	β_0	$n_{\rm f}$	χ^2/ndf
$\langle$Thrust$\rangle$	7.7±1.1±0.2±0.1	4.6±1.3±0.3±0.1	9.2/13
$\langle$C − parameter$\rangle$	7.8±1.0±0.3±0.1	4.7±1.2±0.4±0.1	7.2/13
$\langle M_{\rm h}^2/E_{\rm vis}^2 \rangle$ E def.	7.5±1.5±0.2±0.0	4.8±1.9±0.3±0.0	8.8/13
$\langle M_{\rm s}^2/E_{\rm vis}^2 \rangle$ E def.	7.5±1.1±0.2±0.0	5.0±1.3±0.3±0.1	7.1/13
$\langle B_{\rm max}\rangle$	7.7±1.4±0.1±0.1	4.7±1.9±0.1±0.2	6.3/13
$\langle B_{\rm sum}\rangle$	7.7±0.9±0.1±0.1	4.8±1.2±0.1±0.2	5.9/13
$\langle$Major$\rangle$	8.0±1.1±0.1±0.1	4.3±1.5±0.2±0.2	9.2/13
Weighted Mean	7.7±0.9±0.1±0.1	4.7±1.2±0.1±0.1	
Theory	7.67	5	

Table 10: Results for the fits of β_0 or n_f for different observables with DELPHI data. The first uncertainty is statistical, the second systematic, and the third indicates the uncertainty due to the b–mass correction. Here the minimal uncertainties of the individual observables are taken as uncertainties of the mean value.

The results of the fits to DELPHI data are given in Table 10. The systematic uncertainties of the data are fully propagated. The small uncertainty on the approximately inverse power behaved b–mass correction (see Figure 3) is given separately. Further systematic uncertainties due to the possible presence of small power corrections are not considered here. Contrary to the case of an α_s measurement, this seems to be justified since the energy dependence is even less affected by the power correction. For all observables the results for β_0 or $n_{\rm f}$, are fully consistent with the expected values from QCD. This observation further strengthens the confidence in RGI perturbation theory.

In order to reduce the uncertainty on β_0 or $n_{\rm f}$ more data, especially from low energy experiments, needs to be included to increase the fit range. As $\langle M_{\rm h}^2/E_{\rm vis}^2\rangle$ receives large power corrections due to mass terms, in practice only $\langle 1-T\rangle$ is left over as a possible observable. The data given in [18,41,49] were used in a common fit. As systematic uncertainties of the low energy data cannot be controlled in detail for this fit, systematic and statistical uncertainties were combined leading to small χ^2/ndf values. Thus the uncertainties on the fit values already include systematic components. The fit describes the data very well in the energy range $\sqrt{s} = 14$ to 200 GeV. The slope of the evolution is expected to change at the b production threshold at $\sqrt{s} \simeq 14$ GeV. The central result of the fit is shown in Figure 17 and Table 11. This table also shows the results when the $\langle 1-T\rangle$ data of the experiments are fitted separately. All results are consistent with the QCD expectation within their fit error. In order to estimate a systematic uncertainty of β_0 or $n_{\rm f}$, the measurements of one low energy experiment at a time have been left out from the combined fit. This leads to a maximum deviation from the central fit of $\Delta\beta_0 = +0.11$, $\Delta n_{\rm f} = -0.27$ (excluding PLUTO) and $\Delta\beta_0 = -0.08$, $\Delta n_{\rm f} = +0.17$ (excluding JADE). Adding the fit error and the systematic uncertainty of the DELPHI data in quadrature to the above deviations from the central result leads to the final result:

$$\beta_0 = 7.86 \pm 0.32 \quad ,$$

$$n_{\rm f} = 4.75 \pm 0.44 \quad .$$

These have to be compared with the QCD expectation $\beta_0 = 7.67$ or $n_{\rm f} = 5$.

As a final cross-check of the RGI method one may try to determine the NNLO coefficient ρ_2 (see Equation 25) from a fit to data. Small values of ρ_2 indicate a good approximation of the β-function by the two loop expansion.

As ρ_2 is mainly sensitive to low energy data again only $\langle 1-T\rangle$ is used. Fixing b and ρ_1 to the values expected from QCD a two parameter fit yields:

$$\alpha_s = 0.119 \pm 0.001 \pm 0.001 \quad ,$$

$$\rho_2 = 4 \pm 3 \pm 3.5 \quad .$$

The result for ρ_2 is compatible with zero within its uncertainty, supporting the NLO approximation.

From ρ_2 the expected NNLO coefficient of the $\overline{MS}$ expansion can be deduced:

$$C = 915 \pm 40 \quad .$$

This indicates a sizable correction to the NLO prediction in the $\overline{MS}$ scheme. Even for $\rho_2 = 0$ the NNLO coefficient is large: $C = 882$. Using the Padé estimate for the parameter C leads to a value of $\rho_2 = -10.8$ and a corresponding change of the strong coupling $\Delta\alpha_s = +0.003$ with respect to the case when the NNLO term is omitted.

6.5 Implications for light gluinos

Knowledge of the β function implies model independent limits on the presence of hypothetical particles such as gluinos. Supersymmetric extensions of the standard model predict a weaker energy dependence due to the effect of gluino loops. In testing this hypothesis one should evidently not presume the QCD prediction for β_1 as has been done for the β_0 measurement in the previous section. Instead the full logarithmic energy slope

$$\frac{\mathrm{dR}^{-1}}{\mathrm{d}\ln \mathrm{Q}^2} = -\frac{\beta(R)}{R^2} \tag{32}$$

has to be measured. Evaluating this equation in second order implies a small dependence on $R(Q)$ or the energy respectively. For our measurements the choice of the Z–mass as central scale is reasonable. For $R = \langle 1-T\rangle/A$ one gets:

$$\frac{\mathrm{dR}^{-1}}{\mathrm{d}\ln \mathrm{Q}^2} = 8.32$$

Experiment	β_0	χ^2/ndf	n_f
DELPHI	7.7±1.1 ±0.1	9.22/13	4.6±1.3 ±0.1
L3	10.3±2.3 ±0.0	0.34/4	2.3±2.9 ±0.0
JADE	7.8±0.6 ±0.2	0.92/2	4.8±0.7 ±0.2
TASSO	7.7±1.2 ±0.2	0.02/2	5.0±1.4 ±0.2
PLUTO	8.3±1.3 ±0.2	1.00/4	4.2±1.5 ±0.2
combined	7.86±0.16±0.1	25.7/37	4.75±0.18±0.1
Theory	7.67		5

Table 11: Results for the fit of β_0 for Thrust for different experiments, and as a combined fit. The combined fit includes additionally datapoints from AMY, TOPAZ, MK II and HRS. The first error is statistical, the second is the uncertainty of the b–mass correction

as the QCD prediction. Supersymmetry alters this prediction. The actual value of the logarithmic slope, however, depends on the mass of the additional particles. Gluinos in the mass range from 5 to 190 GeV are excluded from direct searches[1]. Gluinos in the open mass range below 5 GeV can be considered massless compared to the energy range of this experiment. Therefore one expects $\beta_0^{SUSY} = \frac{27-2N_f}{3}$ and $\beta_1^{SUSY} = \frac{81-19N_f}{3}$. This yields the supersymmetry prediction for the logarithmic energy slope of:

$$\frac{\mathrm{dR}^{-1}}{\mathrm{d}\ln \mathrm{Q}^2} = 5.66 \quad .$$

Measuring the slope by fitting the function $1/(a + b\ln Q)$ to the $\frac{\langle 1-T\rangle}{A}$ data yields:

$$\frac{\mathrm{dR}^{-1}}{\mathrm{d}\ln \mathrm{Q}^2} = 8.70 \pm 0.35 \quad .$$

The error contains the statistical and systematic uncertainties in a similar way as discussed for the β_0 measurement in the previous section. The existence of light gluinos can be firmly excluded by our result.

7 Summary and conclusions

Event shape distributions and their means or integrals for the observables $1 - T$, C-Parameter, $B_{\max}$, B_{sum}, EEC, JCEF, the classical and the E- or p-scheme definitions of $M_{\mathrm{h}}^2/E_{\mathrm{vis}}^2$, $M_{\mathrm{s}}^2/E_{\mathrm{vis}}^2$, have been presented in the wide range of hadronic centre-of-mass energies from 45 GeV to 202 GeV. Measurements at energies below $\sqrt{s} = M_Z$ were obtained from events containing a hard radiated photon.

The data can be successfully described over the whole energy range using Monte Carlo fragmentation models or by analytical power correction models. The successful description of the EEC by a power correction ansatz is reported for the first time. Fitting the Dokshitzer–Webber power corrections to event shape distributions yields $\alpha_s = 0.1110 \pm 0.0055_{\mathrm{RMS}}$ and $\alpha_0 = 0.559 \pm 0.073_{\mathrm{RMS}}$. The application to the mean values of event shapes yields $\alpha_s = 0.1217 \pm 0.0046_{\mathrm{RMS}}$ and $\alpha_0 = 0.431 \pm 0.048_{\mathrm{RMS}}$ respectively. A measurement of the shift of the Sudakov shoulder of the C-Parameter indicates an approximately constant power shift over the whole three jet range.

In addition to the comparison of power correction models, the data for inclusive shape means of seven observables depending only on a single energy scale and integrals of the EEC and JCEF have also been compared to results of the so–called Renormalisation Group Invariant, RGI, perturbation theory with and without additional power terms. This method allows for a measurement of β_0 which is independent of any renormalisation scheme or scale. With respect to α_s the RGI prediction is equivalent to the ECH scheme.

It has been observed that RGI perturbation theory is able to describe the energy evolution of these data consistently with a single value of the strong coupling parameter: $\alpha_s(M_Z) = 0.1201 \pm 0.0020_{RMS}$. Within RGI perturbation theory there is no need for power corrections. The small R.M.S. of the α_s values obtained from the different observables indicates an improved decription of the data by RGI perturbation theory compared to the standard $\overline{MS}$ treatment. Furthermore it serves as an important consistency check of the method.

The most important single result of the analysis is the measurement of the β-function of strong interactions. For the leading coefficient , assuming QCD, the average of seven

observables as measured by DELPHI is:

$$\beta_0 = 7.7 \pm 0.9 \pm 0.1 \quad ,$$

where the first uncertainty is statistical and the second systematic. This corresponds to the number of active flavours:

$$n_f = 4.7 \pm 1.2 \pm 0.1 \quad .$$

The systematic uncertainty accounts for experimental uncertainties as well as for the uncertainty induced due to the correction for b hadron decays. Inclusion of additional low energy data for the observable $\langle 1 - T \rangle$ yields the result:

$$\beta_0 = 7.86 \pm 0.32 \quad ,$$

$$n_f = 4.75 \pm 0.44 \quad .$$

Here the uncertainty includes the sources mentioned above as well as an estimate of the systematic error induced by the inclusion of the low energy data.

Within RGI this quantity can be derived without any renormalisation scheme dependence. Power corrections have been found to be negligible. The precision of this result is greatly increased compared to previous determinations of β_0 from event shape observables [49] as well as to a determination based on the most precise measurements of α_s[50]: $\beta_0 = 7.76 \pm 0.44$. Further reduction of the uncertainty is to be expected from a proper combination of the results of the LEP experiments. The analysis should then also be repeated for observables other than $\langle 1 - T \rangle$.

Fitting directly the logarithmic energy slope yields

$$\frac{\mathrm{dR}^{-1}}{\mathrm{d}\ln \mathrm{Q}^2} = \beta(R) = 8.70 \pm 0.35 \quad .$$

This measurement excludes light gluinos in the open mass range below 5 GeV [1] in a model independent way.

Provided the possible presence of power terms in the event shape means is clarified by future studies, the good stability of the results for α_s for a larger number of event shape observable means observed when using RGI perturbation theory may indicate the possibility of improved measurements of the strong coupling α_s.

Acknowledgements

We are greatly indebted to our technical collaborators, to the members of the CERN-SL Division for the excellent performance of the LEP collider, and to the funding agencies for their support in building and operating the DELPHI detector.
We acknowledge in particular the support of
Austrian Federal Ministry of Education, Science and Culture, GZ 616.364/2-III/2a/98,
FNRS–FWO, Flanders Institute to encourage scientific and technological research in the industry (IWT), Belgium,
FINEP, CNPq, CAPES, FUJB and FAPERJ, Brazil,
Czech Ministry of Industry and Trade, GA CR 202/99/1362,
Commission of the European Communities (DG XII),
Direction des Sciences de la Matière, CEA, France,

Bundesministerium für Bildung, Wissenschaft, Forschung und Technologie, Germany,
General Secretariat for Research and Technology, Greece,
National Science Foundation (NWO) and Foundation for Research on Matter (FOM), The Netherlands,
Norwegian Research Council,
State Committee for Scientific Research, Poland, SPUB-M/CERN/PO3/DZ296/2000, SPUB-M/CERN/PO3/DZ297/2000, 2P03B 104 19 and 2P03B 69 23(2002-2004)
JNICT–Junta Nacional de Investigação Científica e Tecnológica, Portugal,
Vedecka grantova agentura MS SR, Slovakia, Nr. 95/5195/134,
Ministry of Science and Technology of the Republic of Slovenia,
CICYT, Spain, AEN99-0950 and AEN99-0761,
The Swedish Natural Science Research Council,
Particle Physics and Astronomy Research Council, UK,
Department of Energy, USA, DE-FG02-01ER41155.
We thank A.A. Pivovarov for numerous enlightening discussions and helpful explanations.

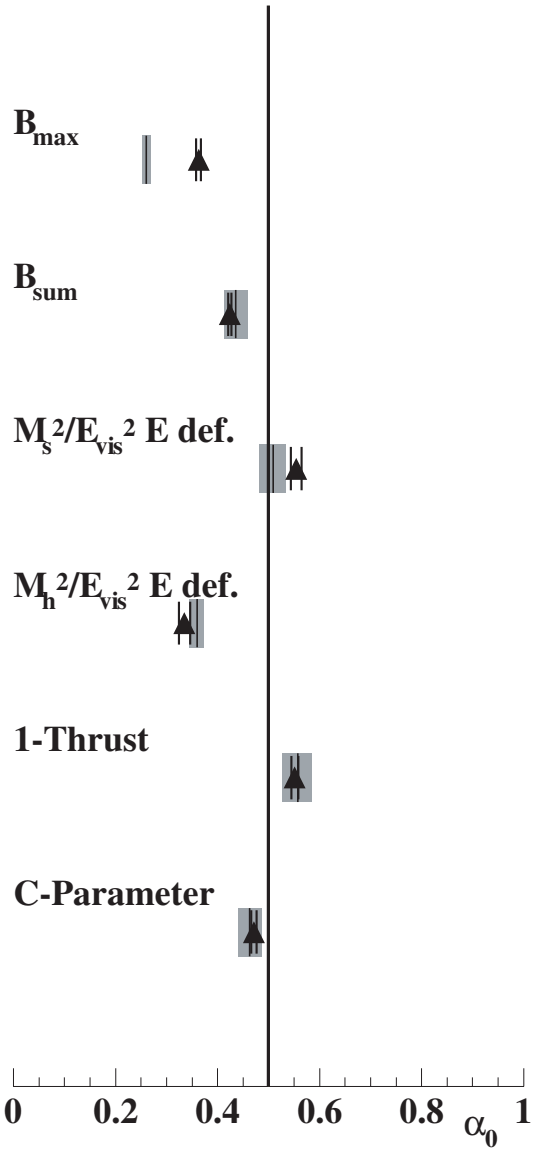

Figure 16: Comparison of the results for α_0 as obtained from fits with fixed $\Lambda_{\overline{MS}} = 0.250$ GeV and the prediction from pure RGI. The shaded bands show the variations due to a change of $\Lambda_{\overline{MS}}$ between 0.220 GeV and 0.280 GeV.

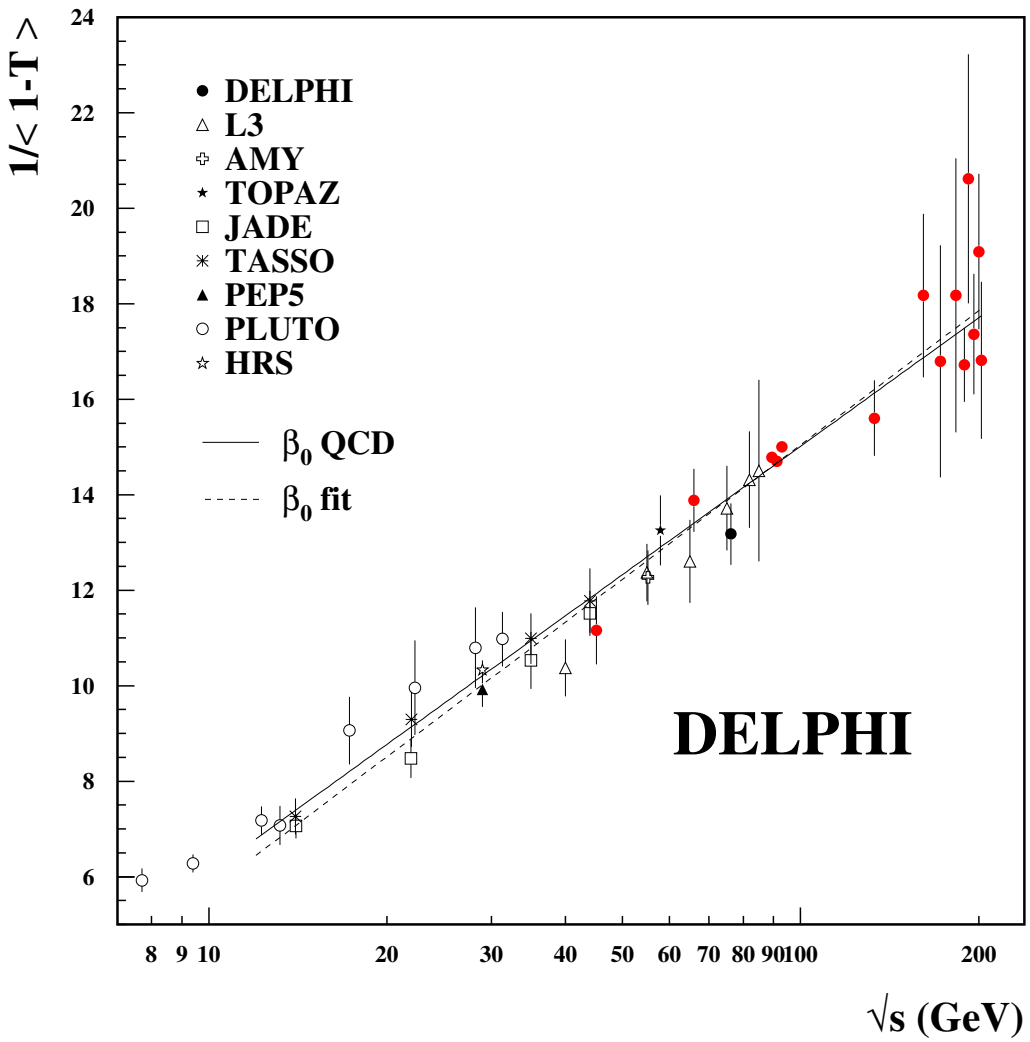

Figure 17: The running of $1/\langle 1-T\rangle$ against $\ln(E_{cm})$. The results of the theoretical prediction and a combined fit of the data of several experiments is shown.

References

[1] D. E. Groom et al. *Eur. Phys. J.* **C15**(2000) 1.
[2] M. Beneke. *Phys. Rep.* **317**(1999) 1.
[3] G. Sterman. (1998) .
[4] A. Dhar. *Phys. Lett.* **B128**(1983) 407.
[5] A. Dhar and V. Gupta. *Phys. Rev.* **D 29**(1984) 2822.
[6] A. Dhar and V. Gupta. *Pramana* **21**(1983) 207.
[7] J. G. Korner, F. Krajewski, and A. A. Pivovarov. *Phys. Rev.* **D63**(2001) 036001.
[8] D.E. Soper and L.R. Surguladze. *Phys. Rev.* **D54**(1996) 4566–4577.
[9] Yu. L. Dokshitzer and B.R. Webber. hep-ph/9704298, 1997.
[10] Yu. L. Dokshitzer et.al. *Nucl. Phys.* **B 511** (1997) 396.
[11] Yu. L. Dokshitzer, et.al. *JHEP* **9805** (1998) 003.
[12] Yu. L. Dokshitzer and B.R. Webber. *Phys. Lett.* **B 352** (1995) 451.
[13] D. Wicke. *Nucl. Phys. Proc. Suppl.***64** (1998) 27.
[14] P. Abreu et al. *Z. Phys.* **C73**(1997) 229–242.
[15] K. Hamacher. *Nucl. Phys.* **B54A (Proc. Suppl.)**(1997) 34–38.
[16] DELPHI Coll., P. Abreu et al. *Nucl. Instr. Meth.* **A303**(1991) 233.
[17] DELPHI Coll., P. Abreu et al. *Nucl. Instr. Meth.* **A378**(1996) 57.
[18] DELPHI Coll., P. Abreu et al. *Phys. Lett.* **B 456**(1999) 322.
[19] D. Wicke. PhD thesis, BUGH Wuppertal, 1999, WU DIS 99-5.
[20] P. Abreu et al. *Nucl. Instrum. Meth.* **A427**(1999) 487–494.
[21] T. Sjostrand et al. *Comput. Phys. Commun.* **135**(2001) 238–259.
[22] DELPHI Coll., P. Abreu et al. *Z. Phys.* **C73**(1996) 11.
[23] E.L. Berger, X. Guo, and J. Qiu. *Phys. Rev.* **D 54**(1996) 5470.
[24] S. Brandt et al. *Phys. Lett.* **15**(1964) 57.
[25] G. Parisi. *Phys. Lett. B* **74**(1978) 65.
[26] L. Clavelli. *Phys. Lett. B* **85**(1979) 111.
[27] S. Catani, G. Turnock, and B. R. Webber. *Phys. Lett.* **B295**(1992) 269.
[28] C.L. Basham et al. *Phys. Rev. Lett.* **41**(1978) 1585.
[29] Y. Ohnishi and H. Masuda SLAC-PUB-6560.
[30] G. P. Salam and D. Wicke. *JHEP* **05**(2001) 061.
[31] Ralf Reinhardt. PhD thesis, BUGH Wuppertal, 2001, WUB-DIS 2001-6. http://elpub.bib.uni-wuppertal.de/edocs/documente/fb08/diss2001/reinhardt/d080113.pdf
[32] Yu.L. Dokshitzer. hep-ph/9911299, 1999.
[33] Yu. L. Dokshitzer, G. Marchesini, G. P. Salam. *Eur. Phys. J. Direct* **C 03**(1999) 1.
[34] Yu. L. Dokshitzer, G. Marchesini, and B. R. Webber. *JHEP* **07**(1999) 012.
[35] S. Catani et al. *Nucl. Phys.* **B 407**(1993) 3.
[36] S. Catani and B.R.Webber. *JHEP* **10**(1997) 005.
[37] B. R. Webber, hep-ph/9510283.
[38] R. K. Ellis, D. A. Ross, and A. E. Terrano. *Nucl. Phys* **B178**(1981) 412.
[39] CERN 89-08 Vol. 1, 1989.
[40] S. Catani and M.H. Seymour. *Phys. Lett. B* **378**(1996) 287.
[41] AMY Coll., Y.K. Li et al. *Phys. Rev.* **D41** (1990) 2675.
HRS Coll., D. Bender et al. *Phys. Rev.* **D31** (1985) 1.
P.A. Movilla Fernandez, et. al. and the JADE Coll. *Eur. Phys. J.* **C1** (1998) 461.
PEP5 Coll., A. Peterson et al. *Phys. Rev.* **D37** (1988) 1.
PLUTO Coll., C. Berger et al. *Z. Phys.* **C12** (1982) 297.

TASSO Coll., W. Braunschweig et al. *Z. Phys.* **C47** (1990) 187.
TOPAZ Coll., Y. Ohnishi et al. *Phys. Lett.* **B313** (1993) 475. .
[42] DELPHI Coll., P. Abreu et al. *Eur. Phys. J.* **C 14**(2000) 557.
[43] G. Grunberg. *Phys. Rev.* **D 29**(1984) 2315.
[44] P. M. Stevenson. *Phys. Rev.* **D 23**(1981) 2916.
[45] M. Beneke. *Phys. Lett.* **B 307**(1993) 154.
[46] C.J. Maxwell, D.T. Barclay, M.T. Reader. *Phys. Rev.* **D 49**(1994) 3480.
[47] W. Celmaster and R. J. Gonzalves. *Phys. Rev.* **D 20**(1979) 1420.
[48] J. M. Campbell, E. W. N. Glover, C. J. Maxwell. *Phys. Rev. Lett.* **81**(1998) 1568.
[49] M. Acciarri et al. *Phys. Lett.* **B 489**(2000) 65–80.
[50] S. Bethke. *J. Phys.* **G26**(2000) R27.